

1 **Characterization of Aerosol Composition, Aerosol Acidity and Organic Acid Partitioning at**  
2 **an Agriculture-Intensive Rural Southeastern U.S. Site**

3  
4 Theodora Nah,<sup>1,a</sup> Hongyu Guo,<sup>1</sup> Amy P. Sullivan,<sup>2</sup> Yunle Chen,<sup>1</sup> David J. Tanner,<sup>1</sup> Athanasios  
5 Nenes,<sup>1,3,4,5</sup> Armistead Russell,<sup>6</sup> Nga Lee Ng,<sup>1,3</sup> L. Gregory Huey<sup>1</sup> and Rodney J. Weber<sup>1,\*</sup>  
6

7 <sup>1</sup>*School of Earth and Atmospheric Sciences, Georgia Institute of Technology, Atlanta, GA, USA*

8 <sup>2</sup>*Department of Atmospheric Science, Colorado State University, Fort Collins, CO, USA*

9 <sup>3</sup>*School of Chemical and Biomolecular Engineering, Georgia Institute of Technology, Atlanta, GA, USA*

10 <sup>4</sup>*ICE-HT, Foundation for Research and Technology, Hellas, 26504 Patras, Greece*

11 <sup>5</sup>*IERSD, National Observatory of Athens, P. Penteli, 15236, Athens, Greece*

12 <sup>6</sup>*School of Civil and Environmental Engineering, Georgia Institute of Technology, Atlanta, GA, USA*

13 <sup>a</sup>*Now at School of Energy and Environment, City University of Hong Kong, Kowloon, Hong Kong, China*

14 \* *To whom correspondence should be addressed: [rweber@eas.gatech.edu](mailto:rweber@eas.gatech.edu)*  
15

16 **Abstract**

17 The implementation of stringent emission regulations has resulted in the decline of anthropogenic  
18 pollutants including sulfur dioxide (SO<sub>2</sub>), nitrogen oxides (NO<sub>x</sub>) and carbon monoxide (CO). In  
19 contrast, ammonia (NH<sub>3</sub>) emissions are largely unregulated, with emissions projected to increase  
20 in the future. We present real-time aerosol and gas measurements from a field study conducted in  
21 an agricultural-intensive region in the southeastern U.S. during the fall of 2016 to investigate how  
22 NH<sub>3</sub> affects particle acidity and secondary organic aerosol (SOA) formation via the gas-particle  
23 partitioning of semi-volatile organic acids. Particle water and pH were determined using the  
24 ISORROPIA-II thermodynamic model and validated by comparing predicted inorganic HNO<sub>3</sub>-  
25 NO<sub>3</sub><sup>-</sup> and NH<sub>3</sub>-NH<sub>4</sub><sup>+</sup> gas-particle partitioning ratios with measured values. Our results showed that  
26 despite the high NH<sub>3</sub> concentrations (average 8.1 ± 5.2 ppb), PM<sub>1</sub> were highly acidic with pH  
27 values ranging from 0.9 to 3.8, and an average pH of 2.2 ± 0.6. PM<sub>1</sub> pH varied by approximately  
28 1.4 units diurnally. Formic and acetic acids were the most abundant gas-phase organic acids, and  
29 oxalate was the most abundant particle-phase water-soluble organic acid anion. Measured particle-  
30 phase water-soluble organic acids were on average 6 % of the total non-refractory PM<sub>1</sub> organic  
31 aerosol mass. The measured molar fraction of oxalic acid in the particle phase (i.e., particle-phase  
32 oxalic acid molar concentration divided by the total oxalic acid molar concentration) ranged  
33 between 47 and 90 % for PM<sub>1</sub> pH 1.2 to 3.4. The measured oxalic acid gas-particle partitioning  
34 ratios were in good agreement with their corresponding thermodynamic predictions, calculated  
35 based on oxalic acid's physicochemical properties, ambient temperature, particle water and pH. In  
36 contrast, gas-particle partitioning of formic and acetic acids were not well predicted for reasons

37 currently unknown. For this study, higher  $\text{NH}_3$  concentrations relative to what has been measured  
38 in the region in previous studies had minor effects on  $\text{PM}_{10}$  organic acids and their influence on the  
39 overall organic aerosol and  $\text{PM}_{10}$  mass concentrations.

## 40 **1. Introduction**

41 Ammonia ( $\text{NH}_3$ ) is the most abundant basic gas in the troposphere and plays an important  
42 role in many atmospheric processes. It is a major neutralizer of atmospheric acidic species, reacting  
43 readily with sulfuric acid ( $\text{H}_2\text{SO}_4$ ) and nitric acid ( $\text{HNO}_3$ ) to form ammonium sulfate and nitrate  
44 salts (e.g.,  $(\text{NH}_4)_2\text{SO}_4$ , and other forms such as  $\text{NH}_4\text{HSO}_4$ ,  $(\text{NH}_4)_3\text{H}(\text{SO}_4)_2$ , and  $\text{NH}_4\text{NO}_3$ ), which  
45 are often the main inorganic components of atmospheric aerosols. The formation of particle-phase  
46 ammonium sulfate and nitrate salts in the aerosol phase depends on the thermodynamic states of  
47 their precursors and the environmental conditions, which can consequently affect aerosol pH. For  
48 example, Guo et al. (2017b) showed that for Southeast U.S. summertime conditions, as aerosol pH  
49 increases, the relative fractions of  $\text{SO}_4^{2-}$  and  $\text{HSO}_4^-$  increases and decreases, respectively. Wet and  
50 dry deposition are the principle  $\text{NH}_3$  sinks (Dentener and Crutzen, 1994).  $\text{NH}_3$  is spatially  
51 heterogeneous, with the highest concentrations typically found near emission sources (Seinfeld  
52 and Pandis, 2016). The dominant  $\text{NH}_3$  sources in rural areas are agricultural in nature, and include  
53 the application of fertilizers and volatilization of livestock waste (Reis et al., 2009; Ellis et al.,  
54 2013; Van Damme et al., 2014). Biomass burning, either from wildfires or from controlled burning  
55 during land-clearing operations, is also a significant source of  $\text{NH}_3$  in rural environments. The  
56 primary source of  $\text{NH}_3$  in urban areas are industrial emissions (e.g.,  $\text{NH}_3$  synthesis, manufacture  
57 of ammonium nitrate and urea, fluid and thermal catalytic cracking processes in petroleum  
58 refinery), though vehicular emissions can be a significant  $\text{NH}_3$  source in some heavily populated  
59 cities (Reis et al., 2009; Lamarque et al., 2010; Yao et al., 2013; Sun et al., 2017). Vehicular  $\text{NH}_3$   
60 emissions are thought to be produced primarily from the reaction of nitrogen oxide with hydrogen  
61 in the presence of carbon monoxide in three-way catalysts of gasoline light duty vehicles (Barbier-  
62 Jr and Duprez, 1994; Whittington et al., 1995; Livingston et al., 2009; Suarez-Bertoa et al., 2014).

63 In the US, implementation of stringent emission controls on traditional anthropogenic air  
64 pollutants, such as sulfur dioxide ( $\text{SO}_2$ ), nitrogen oxides ( $\text{NO}_x$ ) and carbon monoxide ( $\text{CO}$ ), have  
65 led to steady decreases in their emissions, and consequently their concentrations (Blanchard et al.,  
66 2013b; Xing et al., 2013). In contrast,  $\text{NH}_3$  emissions are largely unregulated, and are projected to

67 increase due to increased agricultural operations to feed a growing world population (Reis et al.,  
68 2009; Ellis et al., 2013). Satellite observations showed that gas-phase  $\text{NH}_3$  concentrations have  
69 increased substantially in US agricultural areas from 2002 to 2014 (Warner et al., 2017). More  
70 wildfires from a changing climate, or from controlled burning for land clearing for agricultural  
71 use, may also lead to increased  $\text{NH}_3$  emissions (Reis et al., 2009; Pechony and Shindell, 2010;  
72 Warner et al., 2016). These trends suggest that  $\text{NH}_3$  could play an increasingly important role in  
73 atmospheric chemistry.

74 Previous laboratory studies have shown that  $\text{NH}_3$  can influence secondary organic aerosol  
75 (SOA) formation and processing. For example,  $\text{NH}_3$  increases SOA mass yields in the  $\alpha$ -pinene  
76 ozonolysis system, and is hypothesized to be due to the formation of ammonium salts from the  
77 reaction of  $\text{NH}_3$  with organic acids (Na et al., 2007). The heterogeneous uptake of  $\text{NH}_3$  by SOA  
78 can also lead to the formation of particulate organonitrogen compounds, a class of brown carbon  
79 species that can reduce visibility and impact climate (Laskin et al., 2010; Updyke et al., 2012; Lee  
80 et al., 2013; Laskin et al., 2015).

81 The southeastern U.S. is a natural outdoor laboratory for studying the effects of biogenic-  
82 anthropogenic interactions on atmospheric aerosol formation and processing. Subtropical  
83 vegetation composed mainly of mixed conifer and deciduous forests emit large quantities of  
84 biogenic volatile organic compounds (BVOCs) that can act as precursors for SOA formation  
85 (Blanchard et al., 2011; Guenther et al., 2012; Blanchard et al., 2013a). Large urban centers and  
86 small towns are surrounded by large expanses of forests and widespread rural areas with  
87 agricultural activities. Scattered within the southeastern U.S. are also coal-burning power plants  
88 and industrial facilities. Anthropogenic activities in this region emit large concentrations of VOCs,  
89  $\text{SO}_2$ ,  $\text{NO}_x$ , CO,  $\text{NH}_3$  and aerosols (Blanchard et al., 2013c). Similar to other parts of the U.S.,  $\text{SO}_2$ ,  
90 CO and  $\text{NO}_x$  concentrations have decreased steadily in the southeastern U.S. due to the  
91 implementation of emission controls (Blanchard et al., 2013b). In contrast, gas-phase  $\text{NH}_3$   
92 concentrations have increased in the southeastern U.S. over the same time period (Saylor et al.,  
93 2015). These factors make the southeastern U.S. an intriguing place to study the influence of  $\text{NH}_3$   
94 on atmospheric aerosol chemistry.

95 We performed aerosol and gas measurements during a field study conducted in Yorkville,  
96 Georgia, U.S., in the fall of 2016, with the goal of understanding how  $\text{NH}_3$  affects aerosol acidity

97 and SOA formation. The field site is surrounded by forest and agricultural land, affording an  
98 opportunity to make ambient observations in an area impacted by local emissions of BVOCs and  
99  $\text{NH}_3$ . In this paper, we present gas and aerosol composition measurements that includes a suite of  
100 organic acids. The thermodynamic equilibrium model, ISORROPIA-II, is used to calculate particle  
101 water and pH based on measured inorganic aerosol and gas composition (Nenes et al., 1998;  
102 Fountoukis and Nenes, 2007), and these predictions are compared to observed gas-particle  
103 partitioning of  $\text{NH}_3$ ,  $\text{HNO}_3$  and organic acids. Together, these measurements are used to determine  
104 how aerosol acidity affects the mass concentration of particle-phase organic acids at this site.

## 105 **2. Methods**

### 106 **2.1. Field site**

107 Aerosol and gas measurements were conducted at the Yorkville, Georgia (33.929 N,  
108 85.046 W) SouthEastern Aerosol Research and Characterization (SEARCH) field site from mid-  
109 August to mid-October 2016. This is one of the sampling sites for the Southeastern Center for Air  
110 Pollution and Epidemiology (SCAPE) study where aerosol characterization measurements were  
111 conducted in the summer and winter of 2012 (Xu et al., 2015a; Xu et al., 2015b). A detailed  
112 description of the field site can be found in Hansen et al. (2003) . This rural site is situated in a  
113 mixed forest-agriculture area approximately 55 km northwest and generally upwind of Atlanta.  
114 The immediate surrounding area is used for cattle grazing and poultry concentrated animal feeding  
115 operations (CAFOs) (Fig. S1). There are no major roads near the field site and nearby traffic  
116 emissions were negligible. A large coal-fired power plant (Plant Bowen) is situated approximately  
117 25 km north of the site. Hence, the field site is impacted mainly by BVOC and  $\text{NH}_3$  emissions,  
118 with occasional spikes in  $\text{SO}_2$  and minimal influence from urban anthropogenic pollutants such as  
119  $\text{HNO}_3$ ,  $\text{O}_3$ ,  $\text{NO}_x$  and CO (Fig. S2). The sampling period was characterized by moderate  
120 temperatures (24.0 °C average, 32.6 °C max, 9.5 °C min) and high relative humidities (68.9 % RH  
121 average, 100 % RH max, 21.6 % RH min). Meteorological data are shown in Fig. S3. Data reported  
122 are displayed in eastern daylight time (EDT).

### 123 **2.2. Instrumentation**

124 Instruments were housed in a temperature controlled (~20 °C) trailer during the field study.  
125 Gas-phase  $\text{HNO}_3$ ,  $\text{SO}_2$  and organic acids (formic, acetic, oxalic, butyric, glycolic, propionic,

126 valeric, malonic and succinic acids) were measured by a custom-built chemical ionization mass  
127 spectrometer (CIMS) using sulfur hexafluoride ions ( $\text{SF}_6^-$ ) as reagent ions.  $\text{SO}_2$  and  $\text{HNO}_3$  were  
128 detected as fluoride adducts ( $\text{F}_2\text{SO}_2^-$  and  $\text{NO}_3^- \cdot \text{HF}$ , respectively) while the organic acids (HX) were  
129 detected primarily as conjugated anions ( $\text{X}^-$ ) by the quadrupole mass spectrometer (Huey et al.,  
130 1995; Huey et al., 2004; Nah et al., 2018). This CIMS is referred hereafter as the  $\text{SF}_6$ -CIMS. Gas-  
131 phase  $\text{NH}_3$  was measured by an additional custom-built CIMS using protonated ethanol clusters  
132 ( $(\text{C}_2\text{H}_5\text{OH})_n^+$ ) as reagent ions.  $\text{NH}_3$  was detected primarily as  $\text{NH}_4^+$  ions by the quadrupole mass  
133 spectrometer (Nowak et al., 2002; Yu and Lee, 2012; You et al., 2014a). This CIMS is referred  
134 hereafter as the  $\text{NH}_3$ -CIMS.

135         Since  $\text{HNO}_3$ ,  $\text{NH}_3$  and organic acids may condense on surfaces, both  $\text{SF}_6$ -CIMS and  $\text{NH}_3$ -  
136 CIMS used inlet configurations that minimized wall interactions (Huey et al., 2004; Nowak et al.,  
137 2006). Each CIMS was connected to an inlet (a 7.6 cm ID aluminum pipe) that protruded beyond  
138 the trailer's wall by  $\sim 40$  cm into the ambient air. Both inlets were  $\sim 2$  m above the ground. A donut-  
139 shaped ring was attached to the ambient sampling port of each pipe to curtail the influence of  
140 crosswinds on the pipe's flow dynamics. Both rings were wrapped with a fine wire mesh to prevent  
141 ingestion of insects. A flow of  $\sim 2800$   $\text{L min}^{-1}$  was maintained in each pipe using regenerative  
142 blowers (AMETEK Windjammer 116637-03). Part of this flow ( $7$   $\text{L min}^{-1}$  for the  $\text{SF}_6$ -CIMS and  
143  $4.6$   $\text{L min}^{-1}$  for the  $\text{NH}_3$ -CIMS) was sampled through a custom-made three-way PFA Teflon valve,  
144 which connected the pipe's center to the CIMS sampling orifice and could be switched  
145 automatically between ambient and background measurements.

146         Background measurements were performed every 25 min for 4 min for both the  $\text{SF}_6$ -CIMS  
147 and  $\text{NH}_3$ -CIMS. During each background measurement, the sampled air flow was passed through  
148 an activated charcoal scrubber (Sigma Aldrich) that removed  $\text{SO}_2$ ,  $\text{HNO}_3$  and organic acids prior  
149 to delivery into the  $\text{SF}_6$ -CIMS, and through a silicon phosphate scrubber (Perma Pure Inc.) that  
150 removed  $\text{NH}_3$  prior to delivery into the  $\text{NH}_3$ -CIMS.  $> 99$  % of the targeted species were removed  
151 during background measurements for both the  $\text{SF}_6$ -CIMS and  $\text{NH}_3$ -CIMS. Standard addition  
152 calibrations were performed every 5 h for the  $\text{SF}_6$ -CIMS using the outputs of a 1.12 ppm  $^{34}\text{SO}_2$   
153 gas cylinder (Scott-Marrin Inc.) and a formic or acetic acid permeation device (VICI Metronics).  
154 Calibrations for the other gases measured by the  $\text{SF}_6$ -CIMS were performed in post-field  
155 laboratory work, details of which can be found in Nah et al. (2018) and SI section S1. Standard

156 addition calibrations were performed hourly for the NH<sub>3</sub>-CIMS using the output of a NH<sub>3</sub>  
157 permeation device (KIN-TEK). The outputs of the formic and acetic acid permeation devices were  
158 measured periodically by scrubbing the output of the permeation tube in deionized water, followed  
159 by ion chromatography analysis for formate and acetate. The emission rate of the NH<sub>3</sub> permeation  
160 device was measured using UV optical absorption (Neuman et al., 2003).

161 The detection limits for species measured by the SF<sub>6</sub>-CIMS and NH<sub>3</sub>-CIMS were  
162 approximated from 3 times the standard deviation values ( $3\sigma$ ) of the ion signals measured during  
163 background mode. The detection limits for HNO<sub>3</sub>, SO<sub>2</sub> and the various organic acids measured by  
164 the SF<sub>6</sub>-CIMS ranged from 1 to 60 ppt for 2.5 min integration periods, which corresponded to the  
165 length of a background measurement with a ~4 % duty cycle for each  $m/z$  (Table S1). Measurement  
166 uncertainties for the concentrations of HNO<sub>3</sub>, SO<sub>2</sub> and the various organic acids originate mainly  
167 from calibration measurements, and were between 12 and 25 % (Table S1). The detection limit for  
168 NH<sub>3</sub> measured by the NH<sub>3</sub>-CIMS was 1 ppb for 2.3 min integration periods, which corresponded  
169 to the length of a background measurement with a ~29 % duty cycle for the NH<sub>4</sub><sup>+</sup> ion.  
170 Measurement uncertainties for NH<sub>3</sub> concentrations were 13 %.

171 A high-resolution time-of-flight aerosol mass spectrometer (HR-ToF-AMS, Aerodyne  
172 Research Inc.) was used to measure the elemental composition of ambient non-refractory PM<sub>1</sub>  
173 (particles with aerodynamic diameters < 1 μm). Ambient air was sampled at 16.7 L min<sup>-1</sup> through  
174 a URG PM<sub>1</sub> cyclone and then through a nafion dryer prior to delivery into the HR-ToF-AMS.  
175 Aerosols were dried to RH < 20 % to eliminate the influence of RH on the HR-ToF-AMS's particle  
176 collection efficiency. A detailed description of the HR-ToF-AMS can be found in the literature  
177 (DeCarlo et al., 2006; Canagaratna et al., 2007; Canagaratna et al., 2015). Briefly, the aerodynamic  
178 lens of the HR-ToF-AMS focused the dried submicron aerosols into a narrow beam. The aerosols  
179 were then impacted onto a heated tungsten surface (~600 °C) where they were flash vaporized.  
180 The resulting vapors were ionized by electron impact ionization (70 eV), and the ions were  
181 detected by a time-of-flight mass spectrometer. Gas-phase interferences were accounted for by  
182 subtracting the signals obtained during daily measurements of filtered, particle-free sampling air.  
183 Ionization efficiency calibrations were performed weekly using 300 nm ammonium nitrate and  
184 ammonium sulfate particles. Composition-dependent collection efficiency (CDCE) values of 0.44  
185 to 0.55 were determined using the procedure detailed by Middlebrook et al. (2012), where CDCE

186 values are derived based largely on aerosol inorganic species concentrations and the relative  
187 humidity in the sampling line. In addition, a constant collection efficiency (CE) value of 0.9 was  
188 determined from the comparison of raw HR-ToF-AMS  $\text{SO}_4^{2-}$  data with other particulate  $\text{SO}_4^{2-}$   
189 measurements performed during the study. Comparisons of aerosol mass concentrations obtained  
190 from the application of CDCE values (i.e., 0.44 to 0.55) vs. a constant CE value (i.e., 0.9) to the  
191 raw HR-ToF-AMS data are discussed in section 3.2. Uncertainties in HR-ToF-AMS measurements  
192 were estimated to be approximately 25 % (Canagaratna et al., 2007).

193 Particle-phase water-soluble organic acids, inorganic cations and anions were measured  
194 using two Particle-into-Liquid Sampler (PILS) systems coupled to ion chromatographs (ICs)  
195 (Orsini et al., 2003). Each PILS sampled ambient air at nominally  $16.7 \text{ L min}^{-1}$  through a URG  
196  $\text{PM}_{10}$  cyclone. Before PILS1, which was used to measure water-soluble inorganic cation and  
197 anions, two long (24 cm) URG glass annular denuders coated with sodium carbonate and  
198 phosphorous acid were used to remove acidic and basic gases. Before PILS2, which measured  
199 water-soluble organic acids, a 28 cm parallel plate carbon denuder (Sunset Lab) was used to  
200 remove organic gases (Eatough et al., 1993). In each PILS, aerosols were mixed with water vapor  
201 at  $\sim 100 \text{ }^\circ\text{C}$  generated from heated ultrapure deionized water (Weber et al., 2001; Orsini et al.,  
202 2003). The resulting droplets were impacted onto a plate, with the resulting liquid sample analyzed  
203 by ICs. Each IC system was calibrated at the beginning and end of the study using five multi-  
204 compound standards in order to create calibration curves. Periodically, a HEPA filter (Pall Life  
205 Sciences) was placed on the inlet to determine the background in near real-time. The measurement  
206 uncertainty for each IC system was about 10 %.

207 PILS1 was connected to two Dionex ICS-1500 ICs (Thermo Fisher Scientific) to measure  
208 the water-soluble inorganic ions. These two IC systems include an isocratic pump, self-  
209 regenerating anion or cation suppressor, and conductivity detector. This system will be referred  
210 hereafter as the PILS-IC. Anions were separated using a Dionex IonPac AS15 guard and analytical  
211 column (4 x 250 mm, Thermo Fisher Scientific) employing an eluent of 38 mM sodium hydroxide  
212 at a flow rate of  $1.5 \text{ mL min}^{-1}$ . Cations were separated using a Dionex IonPac CS12A guard and  
213 analytical column (4 x 250 mm, Thermo Fisher Scientific) employing an eluent of 18 mM  
214 methanesulfonic acid at a flow rate of  $1 \text{ mL min}^{-1}$ . A new chromatogram was obtained every 30

215 min with a sample loop fill time (i.e., ambient sample integration time) of 20 min. The limit of  
216 detection for the various anions and cations was approximately  $0.01 \mu\text{g m}^{-3}$ .

217 PILS2 was coupled to a Dionex ICS-4000 capillary high-pressure ion chromatography  
218 (HPIC) system to measure the water-soluble organic acids. The HPIC includes an eluent generator,  
219 isocratic pump, degasser, suppressor, carbonate removal device, and conductivity detector. This  
220 system will be referred hereafter as the PILS-HPIC. The organic acids were separated using a  
221 Dionex AS11-HC- $4\mu\text{m}$  capillary guard and analytical column ( $0.4 \times 250\text{mm}$ , Thermo Fisher  
222 Scientific), which used a potassium hydroxide gradient separation method at a flow rate of  $0.015$   
223  $\text{mL min}^{-1}$ . A new chromatogram was obtained every 60 min with a sample loop fill time of 2 min.  
224 The limit of detection for the various organic acids was approximately  $0.001 \mu\text{g m}^{-3}$ .

225 Particle- and gas-phase water-soluble organic carbon ( $\text{WSOC}_p$  and  $\text{WSOC}_g$ , respectively)  
226 were measured using two Sievers 900 series total organic carbon (TOC) analyzers (GE Analytical  
227 Instruments), as described by Sullivan et al. (2004). For  $\text{WSOC}_p$  measurements, ambient air was  
228 sampled at  $15.2 \text{ L min}^{-1}$  through a URG  $\text{PM}_{10}$  cyclone and a parallel plate carbon denuder into a  
229 PILS coupled to the first TOC analyzer. For  $\text{WSOC}_g$  measurements, ambient air was sampled at  
230  $20 \text{ L min}^{-1}$  through a Teflon filter (45 mm diameter,  $2.0 \mu\text{m}$  pore size, Pall Life Sciences) to remove  
231 particles in the air stream. This filter was changed every 3 to 4 days. The particle-free air was then  
232 directed to a MIST chamber filled with ultrapure deionized water, which scrubbed the soluble  
233 gases at an air flow rate of  $20 \text{ L min}^{-1}$ . Soluble gases with Henry's law constants greater than  $10^3$   
234  $\text{mole L}^{-1} \text{ atm}^{-1}$  were scrubbed into deionized water in the MIST chamber (Spaulding et al., 2002).  
235 The resulting MIST chamber liquid sample was analyzed by the second TOC analyzer. The TOC  
236 analyzers converted the organic carbon in the liquid samples to carbon dioxide using UV radiation  
237 and chemical oxidation. The carbon dioxide formed was then measured by conductivity. The  
238 amount of organic carbon in the liquid samples is proportional to the measured increase in  
239 conductivity of the dissolved carbon dioxide. Each  $\text{WSOC}_p$  and  $\text{WSOC}_g$  measurement lasted 4  
240 min. Background  $\text{WSOC}_p$  and  $\text{WSOC}_g$  measurements were performed for 45 min every 12 h by  
241 stopping the sample air flow and rinsing the system with deionized water. Both TOC analyzers  
242 were calibrated at the beginning and end of the study using varying concentrations of sucrose  
243 solutions to create calibration curves (as specified by the instrument manual). The limit of  
244 detections for  $\text{WSOC}_p$  and  $\text{WSOC}_g$  were  $0.2$  and  $0.4 \mu\text{gC m}^{-3}$ , respectively. The measurement



245 uncertainties for WSOC<sub>p</sub> and WSOC<sub>g</sub> were estimated to be 10 % based on uncertainties in the  
246 TOC analyzer, sample air and liquid flows.

247 A suite of instruments operated by the SEARCH network provided supporting gas and  
248 aerosol measurements (Hansen et al., 2003; Edgerton et al., 2005, 2006). O<sub>3</sub> was measured by a  
249 UV absorption instrument (Thermo Fisher Scientific) with a temporal resolution of 1 min. NO and  
250 NO<sub>x</sub> were measured by a chemiluminescence instrument (Thermo Fisher Scientific) with a  
251 temporal resolution of 1 min. NO<sub>2</sub> was obtained from the difference between NO and NO<sub>x</sub>. CO  
252 was measured by a non-dispersive infrared absorption instrument (Thermo Fisher Scientific) with  
253 a temporal resolution of 1 min. NH<sub>3</sub> was measured by a denuder-based instrument (ARA) with a  
254 temporal resolution of 5 min. Comparisons of measurements by the NH<sub>3</sub>-CIMS and denuder-based  
255 instrument will be presented in section 3.1. A filter-based particle composition monitor (ARA)  
256 provided 24 h-integrated PM<sub>2.5</sub> measurements of particle mass and major inorganic ions measured  
257 offline by ion chromatography. Organic carbon (OC) and elemental carbon (EC) in PM<sub>2.5</sub> were  
258 measured by a OCEC Analyzer (Sunset Labs) with a temporal resolution of 1 h. This analyzer  
259 determined OC by thermal optical transmittance. VOCs were measured by a gas chromatography-  
260 flame ionization detector (GC-FID, Agilent Technologies) with a temporal resolution of 1h.

## 261 **2.2. Particle pH and water calculation**

262 The thermodynamic equilibrium model ISORROPIA-II was used to determine the phase  
263 state and composition of an NH<sub>4</sub><sup>+</sup>-SO<sub>4</sub><sup>2-</sup>-NO<sub>3</sub><sup>-</sup>-Cl<sup>-</sup>-Na<sup>+</sup>-Ca<sup>2+</sup>-K<sup>+</sup>-Mg<sup>2+</sup>-water inorganic aerosol in  
264 equilibrium with its corresponding gas-phase species (Fountoukis and Nenes, 2007; Nenes et al.,  
265 1998). This approach was used in previous studies to determine particle water and pH in different  
266 parts of the world (Guo et al., 2015; Bougiatioti et al., 2016; Guo et al., 2016; Weber et al., 2016;  
267 Guo et al., 2017a; Guo et al., 2017c; Shi et al., 2017). The pH of an aqueous solution is defined as  
268 the negative logarithm of the hydronium ion (H<sub>3</sub>O<sup>+</sup>) activity on a molality basis ([www.goldbook.  
269 iupac.org/html/P/P04524.html](http://www.goldbook.iupac.org/html/P/P04524.html), last access: 6 July 2018):

$$pH = -\log_{10}[a(H^+)] = -\log_{10}[m(H^+)\gamma_m(H^+)/m^\theta] \quad (1a)$$

270 where  $a(H^+)$  is the hydronium ion activity in an aqueous solution,  $m(H^+)$  is the hydronium ion  
271 molality,  $\gamma_m(H^+)$  is the molality-based hydronium ion activity coefficient, and  $m^\theta$  is the standard  
272 molality (1 mol kg<sup>-1</sup>). For simplicity, H<sub>3</sub>O<sup>+</sup> is denoted here as H<sup>+</sup> even though we recognize that

273 the unhydrated hydrogen ion is rare in aqueous solutions. Since most thermodynamic equilibrium  
274 models (e.g., ISORROPIA-II, E-AIM) do not report liquid concentrations, but instead report  
275 species in terms of concentration per volume of air (e.g.,  $\mu\text{g m}^{-3}$ ,  $\mu\text{mol m}^{-3}$ ), we have calculated  
276 the particle pH by:

$$pH = -\log_{10} \gamma_{H^+} H_{aq}^+ = -\log_{10} \frac{1000 \gamma_{H^+} H_{air}^+}{W_i + W_o} \cong -\log_{10} \frac{1000 \gamma_{H^+} H_{air}^+}{W_i} \quad (1b)$$

277 where  $\gamma_{H^+}$  is the hydronium ion activity coefficient (assumed to be 1),  $H_{aq}^+$  is the concentration of  
278 hydronium ions in particle water in mole  $\text{L}^{-1}$  (i.e., the density of water is assumed to be 1000 kg  
279  $\text{m}^{-3}$ , and so pH is calculated in terms of molarity),  $H_{air}^+$  ( $\mu\text{g m}^{-3}$ ) is the hydronium ion concentration  
280 per volume of air, and  $W_i$  and  $W_o$  ( $\mu\text{g m}^{-3}$ ) are the bulk particle water concentrations associated  
281 with inorganic and organic species per volume of air, respectively. In equation 1b, the molecular  
282 weight of  $\text{H}^+$  is taken as 1 g  $\text{mole}^{-1}$ , and 1000 is the factor needed for unit conversion of g  $\text{L}^{-1}$  to  
283  $\mu\text{g m}^{-3}$ .  $H_{air}^+$  and  $W_i$  are outputs of the ISORROPIA-II model. Previous studies have shown that  
284 particle pH values predicted using only  $W_i$  are reasonably accurate since the sensitivity of particle  
285 pH to the effects of  $W_o$  is small (Guo et al., 2015). For the southeastern U.S., Guo et al. (2015)  
286 reported that particle pH values predicted using only  $W_i$  were systematically 0.15 to 0.23 units  
287 lower than those predicted using  $W_i + W_o$  during the 2013 Southern Oxidant Aerosol Study  
288 (SOAS) and SCAPE campaigns. Given this small deviation and that organic aerosol  
289 hygroscopicity was not measured in this field study, we report particle pH only considering  $W_i$ .

290 ISORROPIA-II was run in “forward” mode, which assumes that aerosols are “metastable”  
291 with no solid precipitates, to predict particle pH and the partitioning of semi-volatile compounds.  
292 In “forward” mode, the model calculates the gas-particle equilibrium partitioning concentrations  
293 based on the input of the total concentration of a species (i.e., gas + particle). In “reverse” mode,  
294 the model calculates the gas-particle equilibrium partitioning concentrations based on the input of  
295 only the particle-phase concentration of a species. We used “forward” mode because the “reverse”  
296 mode is sensitive to measurement errors, which often result in large model biases in the predicted  
297 particle pH (Hennigan et al., 2015). The measured particle-phase inorganic  $\text{NH}_4^+$ ,  $\text{SO}_4^{2-}$  and  $\text{NO}_3^-$   
298 concentrations and gas-phase  $\text{HNO}_3$  and  $\text{NH}_3$  concentrations were used as model inputs. The  
299 “metastable” assumption is reasonable since the high RH (average RH 68.9 %) observed during  
300 the study indicated that the aerosols had likely deliquesced. We excluded data for periods where

301 the RH was above 95 % since the exponential growth in particle liquid water with RH introduces  
302 large pH uncertainties (Malm and Day, 2001; Guo et al., 2015).

303 In using ISORROPIA-II to predict particle pH and the partitioning of semi-volatile  
304 compounds, we also assumed that the aerosols are internally mixed and that the particle pH does  
305 not change with particle size (i.e., the overall particle pH is characterized by the particle's bulk  
306 properties). As long as some small fraction of sulfate is mixed with various aerosol components,  
307 (e.g., non-volatile cations), the assumption that aerosols are completely internally mixed has a  
308 small effect on the predicted pH (Guo et al., 2017b). However, the presence of multiple organic  
309 and inorganic species in ambient aerosols may lead to multiple phases within the particle (i.e.,  
310 phase separation). Consequently, this may result in the unequal distribution of inorganic species  
311 among different phases, each with its own water activity and inorganic concentration. Previous  
312 studies have shown that liquid-liquid and solid-liquid phase separations may occur for mixed  
313 organic and inorganic aerosols at low RH and organic aerosol oxygen-to-carbon atomic ratios  
314 (O/C) (Bertram et al., 2011; Song et al., 2012; You et al., 2013; You et al., 2014b; You and  
315 Bertram, 2015). Phase separations were always observed at  $O/C \leq 0.5$ , while no phase separation  
316 was observed at  $O/C \geq 0.8$ . The probability for the occurrence of phase separation decreased at  
317 higher RH for  $0.5 < O/C < 0.8$ . The average O/C for this field study is  $0.69 \pm 0.06$ . Organic acids  
318 were not included in the calculation of particle pH. This is reasonable since their total mass  
319 concentration was small compared to the total inorganic mass concentration. The average ratio of  
320 the organic acid mass concentration to the inorganic mass concentration is 0.25. Furthermore, Song  
321 et al. (2018) showed that including organic acid mass concentrations in thermodynamic model  
322 calculations had minor effects on particle pH if the system is in equilibrium. The validity of these  
323 assumptions and the resulting thermodynamic model predictions will be evaluated by comparing  
324 the predicted gas-particle partitioning ratios of semi-volatile inorganic compounds with measured  
325 values in section 3.3.

### 326 **3. Results and Discussion**

#### 327 **3.1. NH<sub>3</sub> observations**

328 Continuous measurements of NH<sub>3</sub> were made using the NH<sub>3</sub>-CIMS from 13 September to  
329 12 October. Figures 1a and 1b show the time series and average diurnal profile of NH<sub>3</sub>,

330 respectively.  $\text{NH}_3$  concentrations ranged from 0.7 to 39.0 ppb ( $0.5$  to  $28.5 \mu\text{g m}^{-3}$ ), and exhibited  
331 consistent diurnal cycles.  $\text{NH}_3$  was generally higher in the late mornings and early afternoons.  
332 Concentrations started to increase at 07:30, which coincided with an increase in temperature at  
333 sunrise (Fig. S3). Possible reasons for the morning increase include volatilization of particulate  
334 ammonium and animal waste, entrainment from the residual layer where  $\text{NH}_3$  may not have been  
335 depleted, evaporation of dew or fog that contained dissolved  $\text{NH}_3$ , and emission from plant stomata  
336 (Ellis et al., 2011).  $\text{NH}_3$  decreased at 14:30, approximately 1 hour before temperature decreased,  
337 and may be due to changes in the boundary layer height. However, this hypothesis cannot be tested  
338 since the boundary layer height was not measured during the study. The diurnal plot does not  
339 account for dilution as the boundary layer expanded, and only indicates that if emissions were  
340 solely from the surface and lower concentrations aloft, these  $\text{NH}_3$  sources were of significant  
341 magnitude.

342 The average  $\text{NH}_3$  concentration measured by the  $\text{NH}_3$ -CIMS is  $8.1 \pm 5.2$  ppb. This is  
343 approximately 2 times higher than the average  $\text{NH}_3$  concentration ( $3.8 \pm 2.9$  ppb) measured by the  
344 denuder-based instrument operated by the SEARCH network over the same time period (Fig. S4).  
345 Differences in  $\text{NH}_3$  concentrations measured by the two instruments may be due to positive and  
346 negative sampling artifacts caused by differences in sampling inlets (e.g., inlet length and  
347 location), frequency of calibration and background measurements, and (in the case of the denuder-  
348 based instrument) possible sample contamination during chemical analysis. Discussions on how  
349 differences in measured  $\text{NH}_3$  concentrations affect  $\text{PM}_{10}$  pH predictions will be presented in section  
350 3.3. Nevertheless, there is a record of  $\text{NH}_3$  concentrations measured by the denuder-based  
351 instrument at this site since 2008. Just prior to, and during this study,  $\text{NH}_3$  concentrations are  
352 generally the highest observed since 2011 (Fig. S5). These elevated  $\text{NH}_3$  concentrations may be  
353 due to sporadic biomass burning episodes caused by elevated temperatures and widespread  
354 drought across the southeastern U.S. in 2016 (Park Williams et al., 2017; Case and Zavodsky,  
355 2018).

356 The  $\text{NH}_3$ -CIMS measurements are examined with the meteorological data to gain insights  
357 on the primary  $\text{NH}_3$  sources during the sampling period. To account for wind speed, the 1-hour  
358 averaged  $\text{NH}_3$  concentrations are first multiplied by their corresponding 1-hour averaged wind  
359 speeds. These normalized  $\text{NH}_3$  concentrations are then used to construct a wind direction polar

360 plot showing the average normalized  $\text{NH}_3$  concentration per 10 degrees bin (Fig. 1c). The wind  
361 direction polar plot shows that the normalized  $\text{NH}_3$  is approximately 2 times greater than the  
362 average when air masses are transported from the south-east, the general direction of the poultry  
363 CAFOs located approximately 2 km from the field site (Fig. S1), which are known for high  $\text{NH}_3$   
364 emissions. This conclusion is reaffirmed by  $\text{NH}_3$  measurements by the SEARCH network's  
365 denuder-based instrument.

366  $\text{NH}_3$  concentrations measured by the two instruments in this study are substantially higher  
367 than those measured in three recent field studies conducted in the continental U.S.: 2010 California  
368 Nexus (CalNex) study, 2013 Southeast Nexus (SENEX) study and 2013 SOAS study (see Table  
369 1). The differences in  $\text{NH}_3$  may be attributed to differences in land use, proximity to CAFOs and  
370 meteorological conditions. The high  $\text{NH}_3$  concentrations in this study allow us to make ambient  
371 observations of the effect of  $\text{NH}_3$  on particle acidity and the gas-particle partitioning of semi-  
372 volatile inorganic and organic compounds, and compare them with previous studies.

### 373 **3.2. $\text{PM}_1$ composition**

374 The aerosol inorganic chemical composition was measured by several instruments during  
375 this study. The HR-ToF-AMS, PILS-IC and PILS-HPIC measured the composition of  $\text{PM}_1$ , while  
376 a filter-based particle composition monitor measured the composition of  $\text{PM}_{2.5}$ . Comparisons of  
377 aerosol  $\text{SO}_4^{2-}$ ,  $\text{NO}_3^-$  and  $\text{NH}_4^+$  mass concentrations obtained from the application of CDCE values  
378 to the raw HR-ToF-AMS data are compared to those measured by the other three instruments in  
379 Fig. S6.  $\text{NH}_4^+$  measurements by the PILS-IC are not available for comparison due to denuder  
380 breakthrough that occurred during the study.

381  $\text{SO}_4^{2-}$  measurements by the various instruments are generally well correlated with each  
382 other, with  $R^2$  values ranging from 0.64 to 0.92. Although  $\text{PM}_1$   $\text{SO}_4^{2-}$  measurements by the two  
383 PILS systems show good agreement with each other, HR-ToF-AMS CDCE-applied  $\text{SO}_4^{2-}$   
384 measurements are approximately two times higher than the PILS and filter measurements. Similar  
385 systematic differences are also observed for  $\text{NO}_3^-$  and  $\text{NH}_4^+$  measurements.  $\text{NO}_3^-$  and  $\text{NH}_4^+$   
386 measurements by the four instruments are moderately correlated ( $R^2 = 0.54$  to  $0.79$  and  $R^2 = 0.94$ ,  
387 respectively).  $\text{NO}_3^-$  measurements by the PILS and filter systems are mostly similar; however, HR-  
388 ToF-AMS CDCE-applied  $\text{PM}_1$   $\text{NO}_3^-$  and  $\text{NH}_4^+$  measurements are approximately three times and

389 two times higher than the PILS and filter measurements. One possible reason is that the calculated  
390 CDCE is lower due to organics dominating the aerosol composition during the study (average of  
391  $74.2 \pm 7.9$  % of the non-refractory  $PM_1$  mass concentration). Lee et al. (2015) suggested that a  
392 high organic mass fraction may impede the complete efflorescence of aerosols when they are  
393 passed through the drier prior to delivery into the HR-ToF-AMS, thus reducing the particle bounce  
394 and increasing the CE value. Hence, we estimated HR-ToF-AMS  $PM_1$  mass concentrations that  
395 would be consistent with PILS and filter measurements by multiplying all the raw HR-ToF-AMS  
396 data by a constant CE value of 0.9, which was obtained from comparisons of the raw HR-ToF-  
397 AMS  $SO_4^{2-}$  data with PILS-IC and PILS-HPIC  $SO_4^{2-}$  measurements. The constant CE-applied HR-  
398 ToF-AMS data is used in all our subsequent analyses.

399 Figure 2 shows the time series and average diurnal profiles of non-refractory  $PM_1$  species.  
400 The average non-refractory  $PM_1$  organics,  $SO_4^{2-}$ ,  $NO_3^-$  and  $NH_4^+$  mass concentrations are  $5.0 \pm$   
401  $2.3$ ,  $1.6 \pm 0.4$ ,  $0.2 \pm 0.1$  and  $0.4 \pm 0.2$   $\mu g\ m^{-3}$ , respectively. Organics are the dominant non-  
402 refractory  $PM_1$  species, accounting for  $74.2 \pm 7.9$  % of the non-refractory  $PM_1$  mass concentration  
403 during the field study. Organic aerosol mass concentration was slightly higher at night, which is  
404 likely caused by changes in the boundary layer height, emission sources and SOA formation  
405 processes (Xu et al., 2015b). Previous studies have shown that nighttime SOA production in the  
406 Southeastern U.S. is largely attributed to nitrate radical oxidation and ozonolysis of monoterpenes,  
407 which are abundant at night (Pye et al., 2015; Xu et al., 2015a; Xu et al., 2015b; Lee et al., 2016;  
408 Zhang et al., 2018). Specifically, the nitrate radical oxidation of some monoterpenes (e.g.,  $\beta$ -  
409 pinene) could form low volatility organic nitrates that are condensable and could contribute  
410 substantially to the nocturnal organic aerosol mass (Boyd et al., 2015; Boyd et al., 2017; Ng et al.,  
411 2017). Apportionment of organic aerosol sources will be discussed in an upcoming publication.  
412  $SO_4^{2-}$  is the second most abundant non-refractory  $PM_1$  species ( $16.3 \pm 5.7$  % mass fraction),  
413 followed by  $NH_4^+$  ( $5.9 \pm 2$  % mass fraction) and  $NO_3^-$  ( $3.6 \pm 2.2$  % mass fraction).  $SO_4^{2-}$  mass  
414 concentration peaked in the afternoon due to enhanced  $SO_2$  photooxidation (Weber et al., 2003).  
415 The  $NO_3^-$  mass concentration measured by the HR-ToF-AMS is the nitrate functional group (-  
416  $ONO_2$ ) present on organic and inorganic nitrates. Hence, the diurnal profile of the  $NO_3^-$  mass  
417 concentration in Fig. 2 has contributions from both organic and inorganic nitrates. The mass  
418 concentrations of organic and inorganic nitrates increased after sunset and peaked at sunrise (Fig.  
419 S7), likely due to the formation of organic nitrates from nighttime  $NO_3$  chemistry and increased

420 gas-to-particle partitioning of organic and inorganic nitrates as temperature decreased (Xu et al.,  
421 2015a; Xu et al., 2015b). Quantification and characterization of organic nitrates based on HR-ToF-  
422 AMS and PILS-IC PM<sub>1</sub> NO<sub>3</sub><sup>-</sup> measurements will be discussed in a future publication. NH<sub>4</sub><sup>+</sup> mass  
423 concentration has moderate diurnal variations with marginally higher concentrations in the  
424 afternoon, likely due to the contrasting day/night phases of ammonium sulfate and ammonium  
425 nitrate formation. SO<sub>4</sub><sup>2-</sup>, NO<sub>3</sub><sup>-</sup> and NH<sub>4</sub><sup>+</sup> molar concentrations indicated that NH<sub>4</sub><sup>+</sup> is mainly  
426 associated with SO<sub>4</sub><sup>2-</sup> in PM<sub>1</sub>.

### 427 3.3. PM<sub>1</sub> pH predictions

428 CIMS HNO<sub>3</sub> and NH<sub>3</sub> data, HR-ToF-AMS PM<sub>1</sub> SO<sub>4</sub><sup>2-</sup> and NH<sub>4</sub><sup>+</sup> data, PILS-IC PM<sub>1</sub> NO<sub>3</sub><sup>-</sup>  
429 and non-volatile cation (Cl<sup>-</sup>, Na<sup>+</sup>, Ca<sup>2+</sup>, K<sup>+</sup> and Mg<sup>2+</sup>) data, measured temperature and RH are used  
430 as ISORROPIA-II model inputs to predict PM<sub>1</sub>  $W_i$  and pH from 13 September to 6 October. Figure  
431 3 shows the time series and average diurnal profiles of ISORROPIA-predicted PM<sub>1</sub>  $W_i$  and pH.  
432 PM<sub>1</sub> are highly acidic with pH values ranging from 0.9 to 3.8, and an average pH of  $2.2 \pm 0.6$ . The  
433 average PM<sub>1</sub> pH was  $2.5 \pm 0.6$  during periods where the NH<sub>3</sub> concentration was higher than 13.3  
434 ppb (i.e., average NH<sub>3</sub> concentration + 1 standard deviation =  $8.1 + 5.2 = 13.3$  ppb). The PM<sub>1</sub> pH  
435 values in this study are generally similar to those reported by Guo et al. (2015) at the same field  
436 site during winter 2012. Our observation that PM<sub>1</sub> are acidic despite the high NH<sub>3</sub> concentrations  
437 in this study is consistent with previous studies showing that particle pH has weak sensitivities to  
438 wide NH<sub>3</sub> and SO<sub>4</sub><sup>2-</sup> mass concentration ranges due to pH buffering caused by the partitioning of  
439 NH<sub>3</sub> between the gas and particle phases (Weber et al., 2016; Guo et al., 2017c). This weak particle  
440 pH sensitivity also explains the small changes in PM<sub>1</sub> pH values (about 10 % lower, Fig. S8) when  
441 NH<sub>3</sub> measurements by the SEARCH network denuder-based instrument are used in ISORROPIA-  
442 II calculations (instead of NH<sub>3</sub>-CIMS measurements).

443 PM<sub>1</sub> pH varied by approximately 1.4 units throughout the day.  $W_i$  has an average value of  
444  $1.6 \pm 1.7 \mu\text{g m}^{-3}$ . PM<sub>1</sub>  $W_i$  and pH showed similar diurnal profiles, with both peaking in the mid-  
445 morning and reaching their minima in the mid-afternoon. These diurnal trends are consistent with  
446 those previously reported by Guo et al. (2015) for PM<sub>1</sub> measured during the summer and winter in  
447 different parts of the southeastern U.S. Also shown in Fig. 3b is the diurnal profile of  $H_{air}^+$ , which  
448 peaked in the mid-afternoon. The  $W_i$  and  $H_{air}^+$  maximum/minimum ratios are comparable (6.5 and

449 5.3, respectively), thus indicating that the diurnal variation in particle pH is driven by both  $W_i$  and  
450  $H_{air}^+$ .

451 The average  $PM_1$  pH for this study is about 1 unit higher than those for the SENEX and  
452 SOAS campaigns (Table 1), and is likely due to the much higher abundance of  $NH_3$  in this study.  
453 The average  $NH_3$  mass concentration in this study is approximately 49 times and 15 times higher  
454 than those in the SENEX and SOAS campaigns, respectively. The average  $PM_1$  pH for this study  
455 is similar to that for the CalNex campaign even though the average  $NH_3$  mass concentration in this  
456 study is only approximately 4 times higher than that in the CalNex campaign (Guo et al., 2017a).  
457 This may be due, in part, to  $PM_1$   $SO_4^{2-}$  and  $NO_3^-$  mass concentrations at CalNex being  
458 approximately 2 times and 18 times larger than those of this study, respectively. Aerosol inorganic  
459  $SO_4^{2-}$  and  $NO_3^-$  species are hygroscopic species. The much higher  $NO_3^-$  mass concentrations in the  
460 CalNex campaign (due, in part, to high  $NO_x$  emissions) increased particle  $W_i$  substantially, which  
461 diluted  $H^+$  and raised particle pH, resulting in more gas-to-particle partitioning of  $NO_3^-$ , and  
462 eventually leading to pH levels similar to those observed in this study. This type of feedback does  
463 not happen in the southeastern U.S. where non-volatile  $SO_4^{2-}$  dominates the uptake of particle  
464 water. It is also possible that the higher RH and lower temperatures during the CalNex campaign  
465 (relative to this study) contributed to high particle  $W_i$ , which diluted  $H^+$  and raised particle pH  
466 levels similar to those observed in this study.

467 The validity of this study's thermodynamic model predictions is evaluated by comparing  
468 the predicted gas-particle partitioning ratios of semi-volatile inorganic compounds (i.e.,  $NO_3^-$  and  
469  $NH_4^+$ ) with measured values (Fig. S9). CIMS  $HNO_3$  and  $NH_3$  data, PILS-IC  $NO_3^-$  and HR-ToF-  
470 AMS  $NH_4^+$  data are used in this comparison.  $\epsilon(NO_3^-)$  and  $\epsilon(NH_4^+)$  are defined as the particle-phase  
471 molar concentration divided by the total molar concentration (gas + particle), i.e.,  $\epsilon(NO_3^-) = NO_3^-$   
472 / ( $HNO_3 + NO_3^-$ ) and  $\epsilon(NH_4^+) = NH_4^+ / (NH_3 + NH_4^+)$ . Predicted  $NH_3$ ,  $NH_4^+$  and  $\epsilon(NH_4^+)$  values  
473 are generally within 10 % of and are highly correlated ( $R^2 = 0.96$  to  $0.99$ ) with measured values  
474 (Fig. S9). While predicted  $HNO_3$  values generally agreed with measurements, substantial scatter  
475 can be seen between the predicted and measured values for  $NO_3^-$  and  $\epsilon(NO_3^-)$ . This scatter can be  
476 attributed, at least in part, to uncertainties brought about by the low  $PM_1$   $NO_3^-$  mass concentrations  
477 and effects of coarse mode cations (e.g.,  $Na^+$ ,  $Ca^{2+}$ ,  $K^+$  and  $Mg^{2+}$ ) on fine mode  $HNO_3$ - $NO_3^-$  gas-  
478 particle equilibrium (i.e.,  $HNO_3$  can partition to both fine and coarse modes, thereby affecting fine



479 mode  $\text{NO}_3^-$  concentrations; no such effect occurs for  $\text{NH}_3\text{-NH}_4^+$  gas-particle equilibrium). In  
 480 general, the overall good agreement between model predictions and measurements indicated that  
 481 our assumptions that aerosols are metastable (i.e., aerosols are supersaturated aqueous droplets)  
 482 with no phase separation for the thermodynamic calculations are reasonable for the conditions of  
 483 this study, and do not affect model predictions.

484 The molar fractions of  $\text{NO}_3^-$  and  $\text{NH}_4^+$  in the particle phase (i.e.,  $\varepsilon(\text{NO}_3^-)$  and  $\varepsilon(\text{NH}_4^+)$ )  
 485 measured in this study are compared with those measured during the CalNex, SENEX and SOAS  
 486 campaigns. Figure 4 shows the measured  $\varepsilon(\text{NO}_3^-)$  and  $\varepsilon(\text{NH}_4^+)$  values as a function of their  
 487 ISORROPIA-predicted particle pH for the various field studies. For each field study, only a subset  
 488 of the data is chosen for this comparison ( $1 \leq W_i \leq 4 \mu\text{g m}^{-3}$  and  $15 \text{ }^\circ\text{C} \leq \text{temperature} \leq 25 \text{ }^\circ\text{C}$ ) to  
 489 reduce the effects of variability of  $W_i$  and temperature on gas-particle partitioning for comparison  
 490 with the calculated S (or sigmoidal) curves, which are calculated based on  $W_i = 2.5 \mu\text{g m}^{-3}$  and  
 491 temperature =  $20 \text{ }^\circ\text{C}$ . The S curves for  $\text{HNO}_3\text{-NO}_3^-$  and  $\text{NH}_3\text{-NH}_4^+$  partitioning as a function of  
 492 particle pH are also plotted as solid lines. The S curves are calculated based on the solubility and  
 493 dissociation of  $\text{NO}_3^-$  and  $\text{NH}_4^+$  species in water:

$$\varepsilon(\text{NO}_3^-) = \frac{H_{\text{HNO}_3}^* RTW_i \times 0.987 \times 10^{-14}}{\gamma_{\text{H}^+} \gamma_{\text{NO}_3^-} 10^{-\text{pH}} + H_{\text{HNO}_3}^* RTW_i \times 0.987 \times 10^{-14}} \quad (2)$$

$$\varepsilon(\text{NH}_4^+) = \frac{\frac{\gamma_{\text{H}^+} 10^{-\text{pH}}}{\gamma_{\text{NH}_4^+}} H_{\text{NH}_3}^* RTW_i \times 0.987 \times 10^{-14}}{1 + \frac{\gamma_{\text{H}^+} 10^{-\text{pH}}}{\gamma_{\text{NH}_4^+}} H_{\text{NH}_3}^* RTW_i \times 0.987 \times 10^{-14}} \quad (3)$$

494 where  $H_{\text{HNO}_3}^*$  and  $H_{\text{NH}_3}^*$  ( $\text{mole}^2 \text{ kg}^{-2} \text{ atm}^{-1}$ ) are equilibrium constants and are the products of the  
 495 Henry's law constant and the dissociation constant of  $\text{HNO}_3$  and  $\text{NH}_3$ , respectively,  $R$  is the gas  
 496 constant ( $8.314 \text{ m}^3 \text{ Pa K}^{-1} \text{ mol}^{-1}$ ),  $T$  is temperature (K), and  $\gamma_i$ 's are activity coefficients.  $H_{\text{HNO}_3}^*$   
 497 and  $H_{\text{NH}_3}^*$  values at  $20 \text{ }^\circ\text{C}$  are calculated using equations found in Clegg and Brimblecombe (1990)  
 498 and Clegg et al. (1998), respectively. Activity coefficients predicted by ISORROPIA-II are  
 499  $\gamma_{\text{H}^+ - \text{NO}_3^-} = \sqrt{\gamma_{\text{H}^+} \gamma_{\text{NO}_3^-}} = 0.28$ ,  $\gamma_{\text{H}^+} = 1$  and  $\gamma_{\text{NH}_4^+} = 1$ . Derivations of the analytically calculated S  
 500 curves for  $\varepsilon(\text{NO}_3^-)$  and  $\varepsilon(\text{NH}_4^+)$  in equations 2 and 3 can be found in Guo et al. (2017a). As shown  
 501 in Fig. 4, the measured  $\varepsilon(\text{NO}_3^-)$  and  $\varepsilon(\text{NH}_4^+)$  values for the four field studies all generally  
 502 converged on the calculated S curves. The higher particle pH values in this study and the CalNex

503 campaign relative to those for the SENEX and SOAS campaigns resulted in less NH<sub>3</sub> and more  
504 HNO<sub>3</sub> partitioned to the particle phase, as predicted by these simple analytical expressions. A  
505 similar analysis will be performed for the organic acids in section 3.5.

### 506 **3.4. WSOC and water-soluble organic acids**

507 The time series and average diurnal profiles of WSOC<sub>g</sub> and WSOC<sub>p</sub> are shown in Fig. S10.  
508 The average WSOC<sub>g</sub> mass concentration ( $3.6 \pm 2.7 \mu\text{gC m}^{-3}$ ) is roughly four times higher than that  
509 of WSOC<sub>p</sub> ( $1.0 \pm 0.6 \mu\text{gC m}^{-3}$ ). The diurnal profile of WSOC<sub>p</sub> is somewhat flat, likely due to  
510 various organic aerosol sources having different water solubility and diurnal cycles, and  
511 compensating each other throughout the day (Xu et al., 2015b; Xu et al., 2017). In contrast, WSOC<sub>g</sub>  
512 displayed strong diurnal variations. WSOC<sub>g</sub> increased at 07:30, which coincided with the sharp  
513 increase in solar irradiance (Fig. S3). WSOC<sub>g</sub> decreased at 21:30, approximately 2 hours after  
514 sunset. Also shown in Fig. S10 are the time series and average diurnal profile of the mass fraction  
515 of total WSOC in the particle phase, i.e.,  $F_p = \text{WSOC}_p / (\text{WSOC}_p + \text{WSOC}_g)$ . The peak  $F_p$  coincided  
516 with the minima of WSOC<sub>g</sub> at 07:30.

517 The average WSOC<sub>g</sub> and WSOC<sub>p</sub> ( $3.6 \pm 2.7 \mu\text{gC m}^{-3}$  and  $1.0 \pm 0.6 \mu\text{gC m}^{-3}$ ) are slightly  
518 lower than those measured during the SOAS campaign (SOAS WSOC<sub>g</sub> =  $4.9 \mu\text{gC m}^{-3}$  and WSOC<sub>p</sub>  
519 =  $1.7 \mu\text{gC m}^{-3}$ ) (Xu et al., 2017). While the diurnal profiles of WSOC<sub>p</sub> in both studies are flat, the  
520 diurnal profiles of WSOC<sub>g</sub> measured in the two studies are different. WSOC<sub>g</sub> measured in the  
521 SOAS study decreased at sunset, while WSOC<sub>g</sub> measured in this study decreased 2 hours after  
522 sunset. Differences in WSOC<sub>g</sub> diurnal profiles in the two studies are likely due to differences in  
523 emission sources as a result of different sampling periods (SOAS was in early summer and this  
524 study was in early fall), land use and/or land cover. The ratio of WSOC<sub>p</sub> to OC for this study was  
525 estimated at 30 %, but this comparison is imprecise because WSOC<sub>p</sub> was PM<sub>1</sub> and OC was PM<sub>2.5</sub>  
526 (refer to Fig. S11 and SI section S2).

527 Figure 5 shows the time series of particle- and gas-phase concentrations of formic, acetic,  
528 oxalic, malonic, succinic, glutaric and maleic acids. Their diurnal profiles are shown in Fig. 6.  
529 Gas-phase measurements of glutaric and maleic acids are not available. Gas-phase measurements  
530 of butyric, glycolic, propionic and valeric acids were also measured during the study and have

531 been presented in Nah et al. (2018), but will not be discussed here since their particle-phase  
532 measurements are not available.

533 Assuming that all the measured organic acids are completely water-soluble, 30 % of the  
534 WSOC<sub>g</sub> is comprised of these organic acids (Nah et al., 2018). Formic and acetic acids are the  
535 most abundant gas-phase organic acids, with averages of  $2.2 \pm 1.6$  and  $1.9 \pm 1.3 \mu\text{g m}^{-3}$ ,  
536 respectively. The average carbon mass fraction of WSOC<sub>g</sub> comprised of formic and acetic acids  
537 are 7 and 13 %, respectively. All the gas-phase organic acids displayed strong and consistent  
538 diurnal cycles, with higher concentrations being measured during warm and sunny days. Their  
539 concentrations start to increase at sunrise (at 07:30), building to a peak between 15:30 and 19:30,  
540 then decrease overnight.

541 Nah et al. (2018) previously showed that the measured gas-phase organic acids during the  
542 study, including oxalic acid, likely have the same or similar sources. Poor correlations between  
543 gas-phase organic acid concentrations and those of anthropogenic pollutants (HNO<sub>3</sub>, SO<sub>2</sub>, CO and  
544 O<sub>3</sub>) indicated that these organic acids are not due to anthropogenic emissions, and are likely  
545 biogenic in nature. Biogenic emissions of gas-phase organic acids and/or their BVOC precursors  
546 are elevated at high temperatures, resulting in higher organic acid concentrations during warm and  
547 sunny days. For example, isoprene, which is the dominant BVOC in Yorkville, has a somewhat  
548 similar diurnal profile as the organic acids. In addition, the concentration of isoprene is moderately  
549 correlated with those of formic and acetic acids (Fig. S10 of Nah et al., 2018), which are known  
550 products of isoprene photooxidation. Some of these gas-phase organic acids may also be formed  
551 in the particle phase during organic aerosol photochemical aging, with subsequent volatilization  
552 into the gas phase. The gas-particle partitioning of organic acids likely depends on thermodynamic  
553 conditions, which are controlled by particle pH and  $W_i$  and meteorological conditions as will be  
554 shown in section 3.5.

555 The measured particle-phase water-soluble organic acids contributed on average 6 % to the  
556 HR-ToF-AMS-measured organic aerosol mass concentration. The average carbon mass fraction  
557 of WSOC<sub>p</sub> comprised of these organic acids is 4 %. Previous studies have shown that particle-  
558 phase organic acids found in rural environments are oxidation products of gas-phase aliphatic  
559 monocarboxylic acids, which are formed in the photochemical oxidation of biogenic unsaturated  
560 fatty acids and other BVOC precursors (Kawamura and Gagosian, 1987; Kawamura and Ikushima,

561 1993; Kerminen et al., 2000; Kawamura and Bikkina, 2016). These particle-phase organic acids  
562 can also be produced during the multiphase photochemical aging of ambient organic aerosols  
563 (Ervens et al., 2004; Lim et al., 2005; Sorooshian et al., 2007; Sorooshian et al., 2010).

564 Oxalate is the most abundant measured particle-phase water-soluble organic acid anion  
565 (contributing on average 26 % to the total particle-phase organic acid mass concentration), with  
566 mass concentrations ranging from 0.01 to 0.34  $\mu\text{g m}^{-3}$  and a average of  $0.07 \pm 0.05 \mu\text{g m}^{-3}$ . Acetate  
567 (average of  $0.06 \pm 0.03 \mu\text{g m}^{-3}$ ) and formate (average of  $0.05 \pm 0.03 \mu\text{g m}^{-3}$ ) are the second and  
568 third most abundant measured particle-phase water-soluble organic acid anions, respectively.  
569 Particle-phase formate, acetate and maleate showed weak diurnal variations, and may be due, in  
570 part, to various emission sources having different diurnal cycles and compensating each other  
571 throughout the day. Particle-phase oxalate, malonate and succinate peaked in the mid- to late  
572 afternoon, while glutarate generally peaked in the mid-morning. This suggests that while the  
573 production of these organic acids is photochemically-driven, they may have different BVOC  
574 precursors and/or different photochemical production pathways. In addition, since oxalic ( $\text{C}_2$ ),  
575 malonic ( $\text{C}_3$ ), succinic ( $\text{C}_4$ ) and glutaric ( $\text{C}_5$ ) acids belong to the same homologous series of organic  
576 diacids, it is possible that the photochemical aging of particle-phase glutaric acid resulted in the  
577 formation of its successive homologues via the cleavage of C-C bonds. Hence, organic aerosol  
578 photochemical aging may also have contributed to the diurnal profiles of particle-phase oxalate,  
579 malonate, succinate and glutarate.

### 580 **3.5. Gas-particle partitioning of organic acids**

581 The online and simultaneous measurements of gas- and particle-phase organic acid mass  
582 concentrations provided the opportunity to study gas-particle partitioning behavior of semi-volatile  
583 organic compounds with respect to particle pH, as is more commonly done with semi-volatile  
584 inorganic species (see section 3.3). Since formic, acetic and oxalic acids are the three most  
585 abundant measured organic acids present in the gas and particle phases, we focus on the gas-  
586 particle partitioning behaviors of these three organic acids. The average molar fractions ( $\pm 1$   
587 standard deviation) of formic, acetic and oxalic acid in the particle phase (i.e.,  $\epsilon(\text{HCOO}^-)$ ,  
588  $\epsilon(\text{CH}_3\text{CO}_2^-)$  and  $\epsilon(\text{C}_2\text{O}_4^{2-})$ ) are  $3.6 \pm 3.6 \%$ ,  $5.8 \pm 5.0 \%$  and  $73.7 \pm 9.8 \%$ , respectively. The  
589 uncertainties of these ratios for formic, acetic and oxalic acids are 16, 16 and 17 %, respectively,

590 which are obtained from the propagation of their SF<sub>6</sub>-CIMS and PILS-HPIC measurement  
 591 uncertainties.

### 592 3.5.1. Oxalic acid

593 To investigate the factors affecting oxalic acid gas-particle partitioning, the equation for  
 594 the S curve describing the dependence of oxalic acid gas-particle partitioning (i.e.,  $\epsilon(\text{C}_2\text{O}_4^{2-}) =$   
 595  $\text{C}_2\text{O}_4^{2-} / (\text{C}_2\text{H}_2\text{O}_4 + \text{C}_2\text{O}_4^{2-})$ ) on particle pH is derived. As shown in SI section S3, the analytically  
 596 calculated S curve for  $\epsilon(\text{C}_2\text{O}_4^{2-})$  can be simplified to:

$$597 \quad \epsilon(\text{C}_2\text{O}_4^{2-}) \cong \frac{H_{\text{C}_2\text{H}_2\text{O}_4} W_i RT \left( \frac{\gamma_{\text{H}^+} \gamma_{\text{C}_2\text{HO}_4^-}}{\gamma_{\text{C}_2\text{H}_2\text{O}_4}} 10^{-\text{pH} + K_{a1}} \right) \times 0.987 \times 10^{-14}}{\gamma_{\text{H}^+} \gamma_{\text{C}_2\text{HO}_4^-} 10^{-\text{pH}} + H_{\text{C}_2\text{H}_2\text{O}_4} W_i RT \left( \frac{\gamma_{\text{H}^+} \gamma_{\text{C}_2\text{HO}_4^-}}{\gamma_{\text{C}_2\text{H}_2\text{O}_4}} 10^{-\text{pH} + K_{a1}} \right) \times 0.987 \times 10^{-14}} \quad (4)$$

598 where  $H_{\text{C}_2\text{H}_2\text{O}_4}$  (mole L<sup>-1</sup> atm<sup>-1</sup>) is the Henry's law constant for oxalic acid,  $K_{a1}$  (mole L<sup>-1</sup>) is the  
 599 first acid dissociation constant for oxalic acid,  $R$  is the gas constant (8.314 m<sup>3</sup> Pa K<sup>-1</sup> mol<sup>-1</sup>),  $T$  is  
 600 temperature (K), and  $\gamma_i$ 's are activity coefficients. We used the web version of AIOMFAC  
 601 (www.aiomfac.caltech.edu) (Zuend et al., 2008; Zuend et al., 2011; Zuend et al., 2012) to compute  
 602 an average  $\gamma_{\text{C}_2\text{H}_2\text{O}_4}$  value of 0.0492. Since AIOMFAC does not predict  $\gamma_{\text{H}^+} \gamma_{\text{C}_2\text{HO}_4^-}$ , we assumed  
 603 that  $\gamma_{\text{H}^+} \gamma_{\text{C}_2\text{HO}_4^-} = \gamma_{\text{H}^+} \gamma_{\text{NO}_3^-}$ , and used the ISORROPIA-predicted  $\gamma_{\text{H}^+} \gamma_{\text{NO}_3^-}$  value of 0.07. We used  
 604 the average of  $H_{\text{C}_2\text{H}_2\text{O}_4}$  values provided by Clegg et al. (1996), Compernelle and Muller (2014)  
 605 and Saxena and Hildemann (1996) (6.11 x 10<sup>8</sup> mole L<sup>-1</sup> atm<sup>-1</sup> at 25 °C), and accounted for the  
 606 effect of temperature using equation 19 in Sander (2015). Although  $K_{a1}$  also depends on  
 607 temperature, we used the  $K_{a1}$  value at 25 °C (5.62 x 10<sup>-2</sup> mole L<sup>-1</sup>, (Haynes, 2014)) for all the  
 608 oxalic acid S curve calculations since equations that compute  $K_{a1}$  values for pure aqueous oxalic  
 609 acid solutions at different temperatures are not available in the literature. In addition, the  
 610 temperatures observed in this study were close to 25 °C (study-average temperature = 23.4 ± 4.0  
 611 °C).

612 Different S curves for  $\epsilon(\text{C}_2\text{O}_4^{2-})$  are calculated using 1-hour average values obtained from  
 613 the diurnal profiles of temperature and  $W_i$  (specifically at 00:30, 06:30 and 12:30). The shape of  
 614 the S curve changes with the time of day due to the diurnal variations of temperature and  $W_i$  (Fig  
 615 S12 and SI section S3). The S curves for  $\epsilon(\text{C}_2\text{O}_4^{2-})$  are very different from those of other acids,

616 such as  $\varepsilon(\text{NO}_3^-)$  (shown in Fig. 4b). From the S curves for  $\varepsilon(\text{C}_2\text{O}_4^{2-})$ , which are calculated using  
617 conditions in this study, some molar fraction of oxalic acid is always expected to be present in the  
618 particle phase, even at low particle pH (i.e., the S curve does not go to zero at low pH). In contrast,  
619  $\text{HNO}_3$  is expected to be present primarily in the gas phase at low particle pH (i.e.,  $\text{pH} < 1$ ) under  
620 similar temperature and  $W_i$  conditions. This is due primarily to differences in the Henry's law  
621 constants for the two acids.  $H_{\text{HNO}_3}$  ( $2.57 \times 10^5 \text{ mole L}^{-1} \text{ atm}^{-1}$ ) at  $23.4 \text{ }^\circ\text{C}$  is three orders of  
622 magnitude smaller than  $H_{\text{C}_2\text{H}_2\text{O}_4}$  ( $7.27 \times 10^8 \text{ mole L}^{-1} \text{ atm}^{-1}$ ) (Clegg and Brimblecombe, 1990;  
623 Sander, 2015). This means that some undissociated form of oxalate can be found in the particle  
624 phase at any pH, and the molar fraction of this form increases with particle  $W_i$  (see Fig. S12).  
625 Oxalic acid's very high Henry's law constant combined with the  $W_i$  conditions in this study  
626 ensures that some fraction of the organic acid will be in the particle phase regardless the particle  
627 pH.

628 Figure 7 compares the measured  $\varepsilon(\text{C}_2\text{O}_4^{2-})$  vs. ISORROPIA-predicted  $\text{PM}_{10}$  pH to the  
629 analytically calculated S curves(s). The S curve is calculated based on the average temperature and  
630  $W_i$  from 13 September to 6 October ( $23.4 \pm 4.0 \text{ }^\circ\text{C}$  and  $1.6 \pm 1.7 \text{ } \mu\text{g m}^{-3}$ , respectively). We also  
631 calculated the "upper" and "lower" bounds of this S curve based on one standard deviation from  
632 the average temperature and average  $W_i$ . Temperature =  $27.4 \text{ }^\circ\text{C}$  and  $W_i = 0.5 \text{ } \mu\text{g m}^{-3}$  are used for  
633 calculations of the "lower" bound, while temperature =  $19.4 \text{ }^\circ\text{C}$  and  $W_i = 3.3 \text{ } \mu\text{g m}^{-3}$  are used for  
634 calculations of the "upper" bound. For the ambient data, a range in  $W_i$  ( $0.5$  to  $4 \text{ } \mu\text{g m}^{-3}$ ) and  
635 temperature ( $15$  to  $31 \text{ }^\circ\text{C}$ ) is chosen to be close to the analytical calculation. As shown in Fig. 7,  
636 the measured  $\varepsilon(\text{C}_2\text{O}_4^{2-})$  generally converged around the S curve calculated using the average  
637 temperature and  $W_i$  values. Although there is some scatter, the measured ratios are mostly within  
638 the "upper" and "lower" bounds of the S curve.

639 Since the measured  $\varepsilon(\text{C}_2\text{O}_4^{2-})$  are in general agreement with the analytically calculated S  
640 curve (Fig. 7), we can use the S curve to understand qualitatively how high  $\text{NH}_3$  events at the site  
641 affect oxalic acid gas-particle partitioning. Here we define high  $\text{NH}_3$  events as periods where the  
642  $\text{NH}_3$  concentration was higher than  $13.3 \text{ ppb}$  (which is the average  $\text{NH}_3$  concentration + 1 standard  
643 deviation). As discussed in section 3.3, the  $\text{PM}_{10}$  pH during high  $\text{NH}_3$  events is  $2.5 \pm 0.6$ , which is  
644 slightly higher than the average  $\text{PM}_{10}$  pH of  $2.2 \pm 0.6$ . Based on the S curve calculated using the

645 average temperature and  $W_i$  values,  $\epsilon(\text{C}_2\text{O}_4^{2-})$  increases from 81 % to 89 % when particle pH  
646 increases from 2.2 to 2.5. While this result indicates that high  $\text{NH}_3$  concentrations can raise the  
647 particle pH sufficiently such that it can promote gas-to-particle partitioning of oxalic acid, this is  
648 not always the case. Specifically, increasing the particle pH from -2 (or lower) to 1 will not result  
649 in a significant increase in  $\epsilon(\text{C}_2\text{O}_4^{2-})$ . Therefore, whether or not particle pH, and consequently  
650 oxalic acid gas-particle partitioning, is sensitive to  $\text{NH}_3$  concentration depends strongly on particle  
651 pH values.

652 We also examined how well the analytically calculated S curve for  $\epsilon(\text{C}_2\text{O}_4^{2-})$  captures  
653 diurnal variations of the measured  $\epsilon(\text{C}_2\text{O}_4^{2-})$ . The ambient data is divided into two 12 hour sets  
654 (08:00 to 19:59 and 20:00 to 07:59) based on the diurnal profile of solar irradiance. Two S curves  
655 and their corresponding “upper” and “lower” bounds are calculated based on the average  
656 temperature and  $W_i$  of the two data sets, and are subsequently compared to the ambient data. As  
657 shown in Fig. S13, the measured  $\epsilon(\text{C}_2\text{O}_4^{2-})$  in both data sets are generally consistent with predicted  
658 values.

659 A number of inferences can be drawn from the overall good agreement between the  
660 predicted and measured molar fractions of oxalic acid in the particle phase in Figs. 7 and S13. Our  
661 assumptions regarding the activity coefficients, Henry’s law constant and acid dissociation  
662 constants used in the S curve calculations of  $\epsilon(\text{C}_2\text{O}_4^{2-})$  are reasonable for the conditions of this  
663 study (or are at least self-consistent). Analytically calculated S curves are a simple way of  
664 exploring how the gas-particle partitioning of semi-volatile inorganic and organic compounds in  
665 the atmosphere are affected by the compound’s physicochemical properties (e.g., Henry’s law  
666 constants and acid dissociation constants), temperature,  $W_i$  and pH. Overall, these results indicate  
667 that particle-phase oxalate is in equilibrium with gas-phase oxalic acid, and that particle pH can  
668 influence particle-phase oxalate concentrations. It also showed that particle-phase oxalate can be  
669 found over a broad pH range, and that the presence of oxalate does not necessarily provide insights  
670 of the particle pH. Because of its high Henry’s law constant, particle-phase oxalate can be found  
671 in aerosols even at extremely low pH values (i.e., the flat region in Fig. 7), although our data cannot  
672 be used to test this since ambient particle pH values in this study are too high.

### 673 3.5.2 Formic and acetic acids

674 Similar comparisons between the predicted and measured  $\epsilon(\text{HCOO}^-)$  and  $\epsilon(\text{CH}_3\text{CO}_2^-)$  can  
 675 also be made. Derivation of the equations for S curves describing the dependence of formic and  
 676 acetic acid gas-particle partitioning (i.e.,  $\epsilon(\text{HCOO}^-) = \text{HCOO}^- / (\text{HCOOH} + \text{HCOO}^-)$  and  
 677  $\epsilon(\text{CH}_3\text{CO}_2^-) = \text{CH}_3\text{CO}_2^- / (\text{CH}_3\text{CO}_2\text{H} + \text{CH}_3\text{CO}_2^-)$ , respectively) on particle pH are similar to that  
 678 of  $\text{HNO}_3$  since they are monoprotic acids:

$$679 \quad \epsilon(\text{HCOO}^-) = \frac{H_{\text{HCOOH}}W_iRT\left(\frac{\gamma_{\text{H}}+\gamma_{\text{HCOO}^-}}{\gamma_{\text{HCOOH}}}\right)10^{-\text{pH}+K_{a1}}\times 0.987\times 10^{-14}}{\gamma_{\text{H}}+\gamma_{\text{HCOO}^-}10^{-\text{pH}}+H_{\text{HCOOH}}W_iRT\left(\frac{\gamma_{\text{H}}+\gamma_{\text{HCOO}^-}}{\gamma_{\text{HCOOH}}}\right)10^{-\text{pH}+K_{a1}}\times 0.987\times 10^{-14}} \quad (5)$$

$$680 \quad \epsilon(\text{CH}_3\text{CO}_2^-) = \frac{H_{\text{CH}_3\text{CO}_2\text{H}}W_iRT\left(\frac{\gamma_{\text{H}}+\gamma_{\text{CH}_3\text{CO}_2^-}}{\gamma_{\text{CH}_3\text{CO}_2\text{H}}}\right)10^{-\text{pH}+K_{a1}}\times 0.987\times 10^{-14}}{\gamma_{\text{H}}+\gamma_{\text{CH}_3\text{CO}_2^-}10^{-\text{pH}}+H_{\text{CH}_3\text{CO}_2\text{H}}W_iRT\left(\frac{\gamma_{\text{H}}+\gamma_{\text{CH}_3\text{CO}_2^-}}{\gamma_{\text{CH}_3\text{CO}_2\text{H}}}\right)10^{-\text{pH}+K_{a1}}\times 0.987\times 10^{-14}} \quad (6)$$

681 where  $H_{\text{HCOOH}}$  and  $H_{\text{CH}_3\text{CO}_2\text{H}}$  (mole  $\text{L}^{-1}$  atm $^{-1}$ ) are the Henry's law constants for formic and acetic  
 682 acid,  $K_{a1}$ 's (mole  $\text{L}^{-1}$ ) are the first acid dissociation constants,  $R$  is the gas constant (8.314 m $^3$  Pa  
 683  $\text{K}^{-1}$  mol $^{-1}$ ),  $T$  is temperature (K), and  $\gamma_i$ 's are activity coefficients. We used the web version of  
 684 AIOMFAC ([www.aiomfac.caltech.edu](http://www.aiomfac.caltech.edu)) (Zuend et al., 2008; Zuend et al., 2011; Zuend et al., 2012)  
 685 to compute average  $\gamma_{\text{HCOOH}}$  and  $\gamma_{\text{CH}_3\text{COOH}}$  values of 0.334 and 2.150, respectively. Similar to the  
 686 case of oxalic acid, we assumed that  $\gamma_{\text{H}}+\gamma_{\text{HCOO}^-} = \gamma_{\text{H}}+\gamma_{\text{CH}_3\text{COO}^-} = \gamma_{\text{H}}+\gamma_{\text{NO}_3^-}$ , and used the  
 687 ISORROPIA-predicted  $\gamma_{\text{H}}+\gamma_{\text{NO}_3^-}$  value of 0.07. Temperature-dependent  $H_{\text{HCOOH}}$  and  $H_{\text{CH}_3\text{CO}_2\text{H}}$   
 688 values are obtained from Sander (2015) using the same methodology employed to determine  
 689 temperature-dependent  $H_{\text{C}_2\text{H}_2\text{O}_4}$  values. We used  $K_{a1}$  values at 25 °C ( $1.78 \times 10^{-4}$  mole  $\text{L}^{-1}$  for  
 690 formic acid, and  $1.75 \times 10^{-5}$  mole  $\text{L}^{-1}$  for acetic acid (Haynes, 2014)) for the S curve calculations.

691 S curves for  $\epsilon(\text{HCOO}^-)$  and  $\epsilon(\text{CH}_3\text{CO}_2^-)$  calculated based on temperature = 23.4 °C and  $W_i$   
 692 = 1.6  $\mu\text{g m}^{-3}$  can be seen in Fig. 8. Practically no formic or acetic acids are predicted to partition  
 693 to the particle phase (relative to oxalic acid) for the range of  $\text{PM}_1$  pH calculated in this study. This  
 694 is due to significant differences in the Henry's law constants and acid dissociation constants for  
 695 the three organic acids.  $H_{\text{HCOOH}}$  and  $H_{\text{CH}_3\text{CO}_2\text{H}}$  (9540 and 5370 mole  $\text{L}^{-1}$  atm $^{-1}$ , respectively) at 23.4  
 696 °C are substantially smaller than  $H_{\text{C}_2\text{H}_2\text{O}_4}$  ( $7.27 \times 10^8$  mole  $\text{L}^{-1}$  atm $^{-1}$ ) (Sander, 2015). The  $K_{a1}$   
 697 values for formic and acetic acids ( $1.78 \times 10^{-4}$  and  $1.75 \times 10^{-5}$  mole  $\text{L}^{-1}$ , respectively) are also  
 698 considerably smaller than the  $K_{a1}$  value for oxalic acid ( $5.62 \times 10^{-2}$  mole  $\text{L}^{-1}$ ) (Haynes, 2014). Note



699 that  $H_{HNO_3}$  is between that of  $H_{C_2H_2O_4}$  and those of  $H_{HCOOH}$  and  $H_{CH_3CO_2H}$  (compare Fig. 4b with  
700 Figs. 7 and 8).

701 As shown in Fig. 8, higher than expected levels of formate and acetate are observed in the  
702 particle phase. This has also been reported in previous studies (Liu et al., 2012). Laboratory tests  
703 showed that the disagreement cannot be explained by positive biases in the particle-phase formate  
704 and acetate PILS-HPIC measurements resulting from less than 100 % gas removal by the carbon  
705 denuder. The measured denuder efficiency for formic acid was  $\geq 99.97\%$  (SI section S4). The  
706 possibility that formic and acetic acid dimers in the aqueous phase (Schrier et al., 1964; Gilson et  
707 al., 1997; Chen et al., 2008) may result in higher than predicted molar fractions of formate and  
708 acetate in the particle phase was explored, but also could not explain the observed gas-particle  
709 partitioning of these acids (SI section S5). The disagreement could be due to incorrect Henry's law  
710 constants for formic and acetic acids. However, the Henry's law constants for formic and acetic  
711 acid would have to be  $\sim 10^4$  times and  $\sim 3 \times 10^5$  times larger than their literature values, respectively,  
712 in order for their S curves to match our measured molar fractions of formic and acetic acid in the  
713 particle phase. In addition, formic and acetic acids may not be internally mixed with most of the  
714 other PM<sub>1</sub> aerosol components (e.g.,  $SO_4^{2-}$ ,  $NO_3^-$ ,  $NH_4^+$ ,  $C_2O_4^{2-}$ ), and thus are not associated with  
715 acidic aerosols, as assumed above. They may instead be associated with aerosols largely composed  
716 of non-volatile cations and have a pH closer to neutral. More research is needed to explain this  
717 disagreement.

#### 718 4. Summary

719 Gas- and particle-phase measurements were conducted in Yorkville, Georgia (a rural field  
720 site) during fall 2016. The goal of the field study was to understand how NH<sub>3</sub> affects particle  
721 acidity, and consequently SOA formation through the gas-particle partitioning of semi-volatile  
722 inorganic and organic compounds. Since it is a rural site surrounded by forest, agricultural land  
723 and CAFOs, this study provided an opportunity for ambient observations in an area impacted by  
724 high local emissions of BVOCs and NH<sub>3</sub>.

725 NH<sub>3</sub> concentrations measured by the NH<sub>3</sub>-CIMS ranged from 0.7 to 39.0 ppb (average 8.1  
726  $\pm$  5.2 ppb), which were substantially higher than typical levels in the southeastern U.S.. PM<sub>1</sub>  
727 inorganic chemical composition, gas-phase HNO<sub>3</sub> and NH<sub>3</sub> concentrations, temperature and RH

728 were used as model inputs in the ISORROPIA-II thermodynamic model to calculate PM<sub>1</sub> pH and  
729  $W_i$ . PM<sub>1</sub> pH ranged from 0.9 to 3.8, with an average pH of  $2.2 \pm 0.6$ . The measured and predicted  
730 HNO<sub>3</sub>-NO<sub>3</sub><sup>-</sup> and NH<sub>3</sub>-NH<sub>4</sub><sup>+</sup> gas-particle partitioning ratios were in good agreement. The measured  
731 gas-phase organic acids were estimated to contribute 30 % of the overall WSOC<sub>g</sub> on a carbon mass  
732 basis, whereas measured particle-phase organic acids comprised 6 % of the total organic aerosol  
733 mass concentration and 4 % of the overall WSOC<sub>p</sub> on a carbon mass basis. Formic and acetic acids  
734 were the most abundant gas-phase organic acids, with averages of  $2.2 \pm 1.6$  and  $1.9 \pm 1.3$  μg m<sup>-3</sup>,  
735 respectively. Oxalate was the most abundant particle-phase water-soluble organic acid anion, with  
736 a average of  $0.07 \pm 0.05$  μg m<sup>-3</sup>. Measured oxalic acid gas-particle partitioning ratios generally  
737 agreed with analytical predictions, which were based on oxalic acid's physicochemical properties  
738 (specifically, its Henry's law constants, acid dissociation constants and activity coefficients),  
739 temperature,  $W_i$  and particle pH. The partitioning of oxalic acid to the particle phase is highly  
740 sensitive to temperature and  $W_i$ . In contrast, the partitioning of formic and acetic acids to the  
741 particle phase were higher than predicted for reasons currently unknown.

742 Although past air regulations have resulted in decreased sulfate, nitrate and ammonium  
743 aerosol mass concentrations across the U.S., our study suggests that the current limited regulation  
744 of NH<sub>3</sub> emissions may result in some increase in the organic aerosol mass concentration due to  
745 increased gas-to-particle partitioning of some organic acids. However, in this study, the effect was  
746 small since the organic acids comprised a small fraction of the overall organic aerosol mass.

## 747 **5. Acknowledgements**

748 The authors thank Eric Edgerton (Atmospheric Research and Analysis, Inc.) for providing  
749 SEARCH network measurements and meteorological data.

## 750 **6. Funding**

751 This publication was developed under U.S. Environmental Protection Agency (EPA)  
752 STAR Grant R835882 awarded to Georgia Institute of Technology. It has not been formally  
753 reviewed by the EPA. The views expressed in this document are solely those of the authors and  
754 do not necessarily reflect those of the EPA. EPA does not endorse any products or commercial  
755 services mentioned in this publication.

756 **7. Competing financial interests**

757 The authors declare no competing financial interests.

758 **8. Data availability**

759 Data can be accessed by request (rweber@eas.gatech.edu).

760 **9. References**

761 Barbier-Jr, J., and Duprez, D.: Steam Effects in 3-way catalysis, *Applied Catalysis B-*  
762 *Environmental*, 4, 105-140, 10.1016/0926-3373(94)80046-4, 1994.

763 Bertram, A. K., Martin, S. T., Hanna, S. J., Smith, M. L., Bodsworth, A., Chen, Q., Kuwata, M.,  
764 Liu, A., You, Y., and Zorn, S. R.: Predicting the relative humidities of liquid-liquid phase  
765 separation, efflorescence, and deliquescence of mixed particles of ammonium sulfate, organic  
766 material, and water using the organic-to-sulfate mass ratio of the particle and the oxygen-to-carbon  
767 elemental ratio of the organic component, *Atmos. Chem. Phys.*, 11, 10995-11006, 10.5194/acp-  
768 11-10995-2011, 2011.

769 Blanchard, C. L., Hidy, G. M., Tanenbaum, S., and Edgerton, E. S.: NMOC, ozone, and organic  
770 aerosol in the southeastern United States, 1999-2007: 3. Origins of organic aerosol in Atlanta,  
771 Georgia, and surrounding areas, *Atmospheric Environment*, 45, 1291-1302,  
772 10.1016/j.atmosenv.2010.12.004, 2011.

773 Blanchard, C. L., Hidy, G. M., Tanenbaum, S., Edgerton, E. S., and Hartsell, B. E.: The  
774 Southeastern Aerosol Research and Characterization (SEARCH) study: Spatial variations and  
775 chemical climatology, 1999-2010, *Journal of the Air & Waste Management Association*, 63, 260-  
776 275, 10.1080/10962247.2012.749816, 2013a.

777 Blanchard, C. L., Hidy, G. M., Tanenbaum, S., Edgerton, E. S., and Hartsell, B. E.: The  
778 Southeastern Aerosol Research and Characterization (SEARCH) study: Temporal trends in gas  
779 and PM concentrations and composition, 1999-2010, *Journal of the Air & Waste Management*  
780 *Association*, 63, 247-259, 10.1080/10962247.2012.748523, 2013b.

781 Blanchard, C. L., Tanenbaum, S., and Hidy, G. M.: Source Attribution of Air Pollutant  
782 Concentrations and Trends in the Southeastern Aerosol Research and Characterization (SEARCH)  
783 Network, *Environmental Science & Technology*, 47, 13536-13545, 10.1021/es402876s, 2013c.

784 Bougiatioti, A., Nikolaou, P., Stavroulas, I., Kouvarakis, G., Weber, R., Nenes, A., Kanakidou,  
785 M., and Mihalopoulos, N.: Particle water and pH in the eastern Mediterranean: source variability  
786 and implications for nutrient availability, *Atmos. Chem. Phys.*, 16, 4579-4591, 10.5194/acp-16-  
787 4579-2016, 2016.

788 Boyd, C. M., Sanchez, J., Xu, L., Eugene, A. J., Nah, T., Tuet, W. Y., Guzman, M. I., and Ng, N.  
789 L.: Secondary organic aerosol formation from the beta-pinene+NO<sub>3</sub> system: effect of humidity  
790 and peroxy radical fate, *Atmos. Chem. Phys.*, 15, 7497-7522, 10.5194/acp-15-7497-2015, 2015.

791 Boyd, C. M., Nah, T., Xu, L., Berkemeier, T., and Ng, N. L.: Secondary Organic Aerosol (SOA)  
792 from Nitrate Radical Oxidation of Monoterpenes: Effects of Temperature, Dilution, and Humidity  
793 on Aerosol Formation, Mixing, and Evaporation, *Environmental Science & Technology*, 51, 7831-  
794 7841, 10.1021/acs.est.7b01460, 2017.

795 Canagaratna, M. R., Jayne, J. T., Jimenez, J. L., Allan, J. D., Alfarra, M. R., Zhang, Q., Onasch,  
796 T. B., Drewnick, F., Coe, H., Middlebrook, A., Delia, A., Williams, L. R., Trimborn, A. M.,  
797 Northway, M. J., DeCarlo, P. F., Kolb, C. E., Davidovits, P., and Worsnop, D. R.: Chemical and  
798 microphysical characterization of ambient aerosols with the aerodyne aerosol mass spectrometer,  
799 *Mass Spectrometry Reviews*, 26, 185-222, 10.1002/mas.20115, 2007.

800 Canagaratna, M. R., Jimenez, J. L., Kroll, J. H., Chen, Q., Kessler, S. H., Massoli, P., Hildebrandt  
801 Ruiz, L., Fortner, E., Williams, L. R., Wilson, K. R., Surratt, J. D., Donahue, N. M., Jayne, J. T.,  
802 and Worsnop, D. R.: Elemental ratio measurements of organic compounds using aerosol mass  
803 spectrometry: characterization, improved calibration, and implications, *Atmos. Chem. Phys.*, 15,  
804 253-272, 10.5194/acp-15-253-2015, 2015.

805 Case, J. L., and Zavodsky, B. T.: Evolution of 2016 drought in the Southeastern United States from  
806 a Land surface modeling perspective, *Results in Physics*, 8, 654-656, 10.1016/j.rinp.2017.12.029,  
807 2018.

808 Chen, J. H., Brooks, C. L., and Scheraga, H. A.: Revisiting the carboxylic acid dimers in aqueous  
809 solution: Interplay of hydrogen bonding, hydrophobic interactions, and entropy, *Journal of*  
810 *Physical Chemistry B*, 112, 242-249, 10.1021/jp074355h, 2008.

811 Clegg, S. L., and Brimblecombe, P.: Equilibrium partial pressures and mean activity and osmotic  
812 coefficients of 0-100-percent nitric- acid as a function of temperature, *Journal of Physical*  
813 *Chemistry*, 94, 5369-5380, 10.1021/j100376a038, 1990.

814 Clegg, S. L., Brimblecombe, P., and Khan, L.: The Henry's law constant of oxalic acid and its  
815 partitioning into the atmospheric aerosol, *Idojaras*, 100, 51-68, 1996.

816 Clegg, S. L., Brimblecombe, P., and Wexler, A. S.: Thermodynamic model of the system H+  
817 NH<sub>4</sub><sup>+</sup>-SO<sub>4</sub><sup>2-</sup>--NO<sub>3</sub><sup>-</sup>--H<sub>2</sub>O at tropospheric temperatures, *Journal of Physical Chemistry A*, 102,  
818 2137-2154, 10.1021/jp973042r, 1998.

819 DeCarlo, P. F., Kimmel, J. R., Trimborn, A., Northway, M. J., Jayne, J. T., Aiken, A. C., Gonin,  
820 M., Fuhrer, K., Horvath, T., Docherty, K. S., Worsnop, D. R., and Jimenez, J. L.: Field-deployable,  
821 high-resolution, time-of-flight aerosol mass spectrometer, *Analytical Chemistry*, 78, 8281-8289,  
822 10.1021/ac061249n, 2006.

823 Dentener, F. J., and Crutzen, P. J.: A 3-DIMENSIONAL MODEL OF THE GLOBAL AMMONIA  
824 CYCLE, *Journal of Atmospheric Chemistry*, 19, 331-369, 10.1007/bf00694492, 1994.

825 Eatough, D. J., Wadsworth, A., Eatough, D. A., Crawford, J. W., Hansen, L. D., and Lewis, E. A.:  
826 A multiple-system, multi-channel diffusion denuder sampler for the determination of fine-  
827 particulate organic material in the atmosphere, *Atmospheric Environment. Part A. General Topics*,  
828 27, 1213-1219, 10.1016/0960-1686(93)90247-V, 1993.

829 Edgerton, E. S., Hartsell, B. E., Saylor, R. D., Jansen, J. J., Hansen, D. A., and Hidy, G. M.: The  
830 southeastern aerosol research and characterization study: Part II. Filter-based measurements of  
831 fine and coarse particulate matter mass and composition, *Journal of the Air & Waste Management*  
832 *Association*, 55, 1527-1542, 2005.

833 Edgerton, E. S., Hartsell, B. E., Saylor, R. D., Jansen, J. J., Hansen, D. A., and Hidy, G. M.: The  
834 Southeastern Aerosol Research and Characterization Study, part 3: Continuous measurements of

835 fine particulate matter mass and composition, *Journal of the Air & Waste Management*  
836 *Association*, 56, 1325-1341, 10.1080/10473289.2006.10464585, 2006.

837 Edgerton, E. S., Saylor, R. D., Hartsell, B. E., Jansen, J. J., and Hansen, D. A.: Ammonia and  
838 ammonium measurements from the southeastern United States, *Atmospheric Environment*, 41,  
839 3339-3351, 10.1016/j.atmosenv.2006.12.034, 2007.

840 Ellis, R. A., Murphy, J. G., Markovic, M. Z., VandenBoer, T. C., Makar, P. A., Brook, J., and  
841 Mihele, C.: The influence of gas-particle partitioning and surface-atmosphere exchange on  
842 ammonia during BAQS-Met, *Atmos. Chem. Phys.*, 11, 133-145, 10.5194/acp-11-133-2011, 2011.

843 Ellis, R. A., Jacob, D. J., Sulprizio, M. P., Zhang, L., Holmes, C. D., Schichtel, B. A., Blett, T.,  
844 Porter, E., Pardo, L. H., and Lynch, J. A.: Present and future nitrogen deposition to national parks  
845 in the United States: critical load exceedances, *Atmos. Chem. Phys.*, 13, 9083-9095, 10.5194/acp-  
846 13-9083-2013, 2013.

847 Ervens, B., Feingold, G., Frost, G. J., and Kreidenweis, S. M.: A modeling study of aqueous  
848 production of dicarboxylic acids: 1. Chemical pathways and speciated organic mass production,  
849 *Journal of Geophysical Research-Atmospheres*, 109, 10.1029/2003jd004387, 2004.

850 Fountoukis, C., and Nenes, A.: ISORROPIA II: a computationally efficient thermodynamic  
851 equilibrium model for  $K^+-Ca^{2+}-Mg^{2+}-NH_4^+-Na^+-SO_4^{2-}-NO_3^- -Cl^- -H_2O$  aerosols, *Atmos.*  
852 *Chem. Phys.*, 7, 4639-4659, 2007.

853 Gilson, M. K., Given, J. A., Bush, B. L., and McCammon, J. A.: The statistical-thermodynamic  
854 basis for computation of binding affinities: A critical review, *Biophysical Journal*, 72, 1047-1069,  
855 10.1016/s0006-3495(97)78756-3, 1997.

856 Guenther, A. B., Jiang, X., Heald, C. L., Sakulyanontvittaya, T., Duhl, T., Emmons, L. K., and  
857 Wang, X.: The Model of Emissions of Gases and Aerosols from Nature version 2.1 (MEGAN2.1):  
858 an extended and updated framework for modeling biogenic emissions, *Geoscientific Model*  
859 *Development*, 5, 1471-1492, 10.5194/gmd-5-1471-2012, 2012.

860 Guo, H., Xu, L., Bougiatioti, A., Cerully, K. M., Capps, S. L., Hite, J. R., Jr., Carlton, A. G., Lee,  
861 S. H., Bergin, M. H., Ng, N. L., Nenes, A., and Weber, R. J.: Fine-particle water and pH in the

862 southeastern United States, *Atmos. Chem. Phys.*, 15, 5211-5228, 10.5194/acp-15-5211-2015,  
863 2015.

864 Guo, H., Sullivan, A. P., Campuzano-Jost, P., Schroder, J. C., Lopez-Hilfiker, F. D., Dibb, J. E.,  
865 Jimenez, J. L., Thornton, J. A., Brown, S. S., Nenes, A., and Weber, R. J.: Fine particle pH and  
866 the partitioning of nitric acid during winter in the northeastern United States, *Journal of*  
867 *Geophysical Research-Atmospheres*, 121, 10355-10376, 10.1002/2016jd025311, 2016.

868 Guo, H., Liu, J. M., Froyd, K. D., Roberts, J. M., Veres, P. R., Hayes, P. L., Jimenez, J. L., Nenes,  
869 A., and Weber, R. J.: Fine particle pH and gas-particle phase partitioning of inorganic species in  
870 Pasadena, California, during the 2010 CalNex campaign, *Atmos. Chem. Phys.*, 17, 5703-5719,  
871 10.5194/acp-17-5703-2017, 2017a.

872 Guo, H., Nenes, A., and Weber, R. J.: The underappreciated role of nonvolatile cations on aerosol  
873 ammonium-sulfate molar ratios, *Atmos. Chem. Phys. Discuss.*, 2017, 1-19, 10.5194/acp-2017-  
874 737, 2017b.

875 Guo, H., Weber, R. J., and Nenes, A.: High levels of ammonia do not raise fine particle pH  
876 sufficiently to yield nitrogen oxide-dominated sulfate production, *Scientific Reports*, 7,  
877 10.1038/s41598-017-11704-0, 2017c.

878 Hansen, D. A., Edgerton, E. S., Hartsell, B. E., Jansen, J. J., Kandasamy, N., Hidy, G. M., and  
879 Blanchard, C. L.: The southeastern aerosol research and characterization study: Part 1-overview,  
880 *Journal of the Air & Waste Management Association*, 53, 1460-1471, 2003.

881 Haynes, W. M.: *CRC handbook of chemistry and physics: A ready-reference book of chemical*  
882 *and physical data.* , Boca Raton: CRC Press, 2014.

883 Hennigan, C. J., Izumi, J., Sullivan, A. P., Weber, R. J., and Nenes, A.: A critical evaluation of  
884 proxy methods used to estimate the acidity of atmospheric particles, *Atmos. Chem. Phys.*, 15,  
885 2775-2790, 10.5194/acp-15-2775-2015, 2015.

886 Huey, L. G., Hanson, D. R., and Howard, C. J.: Reactions of SF<sub>6</sub>- and I- with Atmospheric Trace  
887 Gases, *Journal of Physical Chemistry*, 99, 5001-5008, 10.1021/j100014a021, 1995.

888 Huey, L. G., Tanner, D. J., Slusher, D. L., Dibb, J. E., Arimoto, R., Chen, G., Davis, D., Buhr, M.  
889 P., Nowak, J. B., Mauldin, R. L., Eisele, F. L., and Kosciuch, E.: CIMS measurements of HNO<sub>3</sub>  
890 and SO<sub>2</sub> at the South Pole during ISCAT 2000, *Atmospheric Environment*, 38, 5411-5421,  
891 10.1016/j.atmosenv.2004.04.037, 2004.

892 Kawamura, K., and Gagosian, R. B.: Implication of omega-oxocarboxylic acids in the remote  
893 marine atmosphere for photo-oxidation of unsaturated fatty acids, *Nature*, 325, 330-332,  
894 10.1038/325330a0, 1987.

895 Kawamura, K., and Ikushima, K.: Seasonal changes in the distribution of dicarboxylic acids in the  
896 urban atmosphere, *Environmental Science & Technology*, 27, 2227-2235, 10.1021/es00047a033,  
897 1993.

898 Kawamura, K., and Bikkina, S.: A review of dicarboxylic acids and related compounds in  
899 atmospheric aerosols: Molecular distributions, sources and transformation, *Atmospheric Research*,  
900 170, 140-160, 10.1016/j.atmosres.2015.11.018, 2016.

901 Kerminen, V. M., Ojanen, C., Pakkanen, T., Hillamo, R., Aurela, M., and Merilainen, J.: Low-  
902 molecular-weight dicarboxylic acids in an urban and rural atmosphere, *Journal of Aerosol Science*,  
903 31, 349-362, 10.1016/s0021-8502(99)00063-4, 2000.

904 Lamarque, J. F., Bond, T. C., Eyring, V., Granier, C., Heil, A., Klimont, Z., Lee, D., Liousse, C.,  
905 Mieville, A., Owen, B., Schultz, M. G., Shindell, D., Smith, S. J., Stehfest, E., Van Aardenne, J.,  
906 Cooper, O. R., Kainuma, M., Mahowald, N., McConnell, J. R., Naik, V., Riahi, K., and van  
907 Vuuren, D. P.: Historical (1850-2000) gridded anthropogenic and biomass burning emissions of  
908 reactive gases and aerosols: methodology and application, *Atmos. Chem. Phys.*, 10, 7017-7039,  
909 10.5194/acp-10-7017-2010, 2010.

910 Laskin, A., Laskin, J., and Nizkorodov, S. A.: Chemistry of Atmospheric Brown Carbon, *Chemical*  
911 *Reviews*, 115, 4335-4382, 10.1021/cr5006167, 2015.

912 Laskin, J., Laskin, A., Roach, P. J., Slysz, G. W., Anderson, G. A., Nizkorodov, S. A., Bones, D.  
913 L., and Nguyen, L. Q.: High-Resolution Desorption Electrospray Ionization Mass Spectrometry



914 for Chemical Characterization of Organic Aerosols, *Analytical Chemistry*, 82, 2048-2058,  
915 10.1021/ac902801f, 2010.

916 Lee, B. H., Mohr, C., Lopez-Hilfiker, F. D., Lutz, A., Hallquist, M., Lee, L., Romer, P., Cohen, R.  
917 C., Iyer, S., Kurten, T., Hu, W. W., Day, D. A., Campuzano-Jost, P., Jimenez, J. L., Xu, L., Ng,  
918 N. L., Guo, H. Y., Weber, R. J., Wild, R. J., Brown, S. S., Koss, A., de Gouw, J., Olson, K.,  
919 Goldstein, A. H., Seco, R., Kim, S., McAvey, K., Shepson, P. B., Starn, T., Baumann, K.,  
920 Edgerton, E. S., Liu, J. M., Shilling, J. E., Miller, D. O., Brune, W., Schobesberger, S., D'Ambro,  
921 E. L., and Thornton, J. A.: Highly functionalized organic nitrates in the southeast United States:  
922 Contribution to secondary organic aerosol and reactive nitrogen budgets, *Proceedings of the*  
923 *National Academy of Sciences of the United States of America*, 113, 1516-1521,  
924 10.1073/pnas.1508108113, 2016.

925 Lee, B. P., Li, Y. J., Yu, J. Z., Louie, P. K. K., and Chan, C. K.: Characteristics of submicron  
926 particulate matter at the urban roadside in downtown Hong Kong-Overview of 4 months of  
927 continuous high-resolution aerosol mass spectrometer measurements, *Journal of Geophysical*  
928 *Research-Atmospheres*, 120, 7040-7058, 10.1002/2015jd023311, 2015.

929 Lee, H. J., Laskin, A., Laskin, J., and Nizkorodov, S. A.: Excitation-Emission Spectra and  
930 Fluorescence Quantum Yields for Fresh and Aged Biogenic Secondary Organic Aerosols,  
931 *Environmental Science & Technology*, 47, 5763-5770, 10.1021/es400644c, 2013.

932 Lim, H. J., Carlton, A. G., and Turpin, B. J.: Isoprene forms secondary organic aerosol through  
933 cloud processing: Model simulations, *Environmental Science & Technology*, 39, 4441-4446,  
934 10.1021/es048039h, 2005.

935 Liu, J., Zhang, X., Parker, E. T., Veres, P. R., Roberts, J. M., de Gouw, J. A., Hayes, P. L., Jimenez,  
936 J. L., Murphy, J. G., Ellis, R. A., Huey, L. G., and Weber, R. J.: On the gas-particle partitioning of  
937 soluble organic aerosol in two urban atmospheres with contrasting emissions: 2. Gas and particle  
938 phase formic acid, *Journal of Geophysical Research-Atmospheres*, 117, 10.1029/2012jd017912,  
939 2012.

940 Livingston, C., Rieger, P., and Winer, A.: Ammonia emissions from a representative in-use fleet  
941 of light and medium-duty vehicles in the California South Coast Air Basin, *Atmospheric*  
942 *Environment*, 43, 3326-3333, 10.1016/j.atmosenv.2009.04.009, 2009.

943 Malm, W. C., and Day, D. E.: Estimates of aerosol species scattering characteristics as a function  
944 of relative humidity, *Atmospheric Environment*, 35, 2845-2860, 10.1016/s1352-2310(01)00077-  
945 2, 2001.

946 Middlebrook, A. M., Bahreini, R., Jimenez, J. L., and Canagaratna, M. R.: Evaluation of  
947 Composition-Dependent Collection Efficiencies for the Aerodyne Aerosol Mass Spectrometer  
948 using Field Data, *Aerosol Science and Technology*, 46, 258-271, 10.1080/02786826.2011.620041,  
949 2012.

950 Na, K., Song, C., Switzer, C., and Cocker, D. R.: Effect of ammonia on secondary organic aerosol  
951 formation from alpha-Pinene ozonolysis in dry and humid conditions, *Environmental Science &*  
952 *Technology*, 41, 6096-6102, 10.1021/es061956y, 2007.

953 Nah, T., Ji, Y., Tanner, D. J., Guo, H., Sullivan, A. P., Ng, N. L., Weber, R. J., and Huey, L. G.:  
954 Real-time measurements of gas-phase organic acids using SF<sub>6</sub>- chemical ionization mass  
955 spectrometry, *Atmos. Meas. Tech. Discuss.*, 2018, 1-40, 10.5194/amt-2018-46, 2018.

956 Nenes, A., Pandis, S. N., and Pilinis, C.: ISORROPIA: A new thermodynamic equilibrium model  
957 for multiphase multicomponent inorganic aerosols, *Aquatic Geochemistry*, 4, 123-152,  
958 10.1023/a:1009604003981, 1998.

959 Neuman, J. A., Ryerson, T. B., Huey, L. G., Jakoubek, R., Nowak, J. B., Simons, C., and  
960 Fehsenfeld, F. C.: Calibration and evaluation of nitric acid and ammonia permeation tubes by UV  
961 optical absorption, *Environmental Science & Technology*, 37, 2975-2981, 10.1021/es0264221,  
962 2003.

963 Ng, N. L., Brown, S. S., Archibald, A. T., Atlas, E., Cohen, R. C., Crowley, J. N., Day, D. A.,  
964 Donahue, N. M., Fry, J. L., Fuchs, H., Griffin, R. J., Guzman, M. I., Herrmann, H., Hodzic, A.,  
965 Iinuma, Y., Jimenez, J. L., Kiendler-Scharr, A., Lee, B. H., Luecken, D. J., Mao, J. Q., McLaren,  
966 R., Mutzel, A., Osthoff, H. D., Ouyang, B., Picquet-Varrault, B., Platt, U., Pye, H. O. T., Rudich,

967 Y., Schwantes, R. H., Shiraiwa, M., Stutz, J., Thornton, J. A., Tilgner, A., Williams, B. J., and  
968 Zaveri, R. A.: Nitrate radicals and biogenic volatile organic compounds: oxidation, mechanisms,  
969 and organic aerosol, *Atmos. Chem. Phys.*, 17, 2103-2162, 10.5194/acp-17-2103-2017, 2017.

970 Nowak, J. B., Huey, L. G., Eisele, F. L., Tanner, D. J., Mauldin, R. L., Cantrell, C., Kosciuch, E.,  
971 and Davis, D. D.: Chemical ionization mass spectrometry technique for detection of  
972 dimethylsulfoxide and ammonia, *Journal of Geophysical Research-Atmospheres*, 107,  
973 10.1029/2001jd001058, 2002.

974 Nowak, J. B., Huey, L. G., Russell, A. G., Tian, D., Neuman, J. A., Orsini, D., Sjostedt, S. J.,  
975 Sullivan, A. P., Tanner, D. J., Weber, R. J., Nenes, A., Edgerton, E., and Fehsenfeld, F. C.:  
976 Analysis of urban gas phase ammonia measurements from the 2002 Atlanta Aerosol Nucleation  
977 and Real-Time Characterization Experiment (ANARChE), *Journal of Geophysical Research-*  
978 *Atmospheres*, 111, 14, 10.1029/2006jd007113, 2006.

979 Orsini, D. A., Ma, Y. L., Sullivan, A., Sierau, B., Baumann, K., and Weber, R. J.: Refinements to  
980 the particle-into-liquid sampler (PILS) for ground and airborne measurements of water soluble  
981 aerosol composition, *Atmospheric Environment*, 37, 1243-1259, 10.1016/s1352-2310(02)01015-  
982 4, 2003.

983 Park Williams, A., Cook, B. I., Smerdon, J. E., Bishop, D. A., Seager, R., and Mankin, J. S.: The  
984 2016 Southeastern U.S. Drought: An Extreme Departure From Centennial Wetting and Cooling,  
985 *Journal of Geophysical Research: Atmospheres*, 122, 8888-8905, 10.1002/2017JD027523,  
986 2017.

987 Pechony, O., and Shindell, D. T.: Driving forces of global wildfires over the past millennium and  
988 the forthcoming century, *Proceedings of the National Academy of Sciences of the United States*  
989 *of America*, 107, 19167-19170, 10.1073/pnas.1003669107, 2010.

990 Pye, H. O. T., Luecken, D. J., Xu, L., Boyd, C. M., Ng, N. L., Baker, K. R., Ayres, B. R., Bash, J.  
991 O., Baumann, K., Carter, W. P. L., Edgerton, E., Fry, J. L., Hutzell, W. T., Schwede, D. B., and  
992 Shepson, P. B.: Modeling the Current and Future Roles of Particulate Organic Nitrates in the  
993 Southeastern United States, *Environmental Science & Technology*, 49, 14195-14203,  
994 10.1021/acs.est.5b03738, 2015.

995 Reis, S., Pinder, R. W., Zhang, M., Lijie, G., and Sutton, M. A.: Reactive nitrogen in atmospheric  
996 emission inventories, *Atmos. Chem. Phys.*, 9, 7657-7677, 10.5194/acp-9-7657-2009, 2009.

997 Sander, R.: Compilation of Henry's law constants (version 4.0) for water as solvent, *Atmos. Chem.*  
998 *Phys.*, 15, 4399-4981, 10.5194/acp-15-4399-2015, 2015.

999 Saxena, P., and Hildemann, L. M.: Water-soluble organics in atmospheric particles: A critical  
1000 review of the literature and application of thermodynamics to identify candidate compounds,  
1001 *Journal of Atmospheric Chemistry*, 24, 57-109, 10.1007/bf00053823, 1996.

1002 Saylor, R., Myles, L., Sibble, D., Caldwell, J., and Xing, J.: Recent trends in gas-phase ammonia  
1003 and PM<sub>2.5</sub> ammonium in the Southeast United States, *Journal of the Air & Waste Management*  
1004 *Association*, 65, 347-357, 10.1080/10962247.2014.992554, 2015.

1005 Schrier, E. E., Pottle, M., and Scheraga, H. A.: The Influence of Hydrogen and Hydrophobic Bonds  
1006 on the Stability of the Carboxylic Acid Dimers in Aqueous Solution, *Journal of the American*  
1007 *Chemical Society*, 86, 3444-3449, 10.1021/ja01071a009, 1964.

1008 Seinfeld, J. H., and Pandis, S. N.: *Atmospheric chemistry and physics : from air pollution to*  
1009 *climate change*, Third edition. ed., John Wiley & Sons, Inc., Hoboken, New Jersey, xxvi, 1120  
1010 pages pp., 2016.

1011 Shi, G. L., Xu, J., Peng, X., Xiao, Z. M., Chen, K., Tian, Y. Z., Guan, X. B., Feng, Y. C., Yu, H.  
1012 F., Nenes, A., and Russell, A. G.: pH of Aerosols in a Polluted Atmosphere: Source Contributions  
1013 to Highly Acidic Aerosol, *Environmental Science & Technology*, 51, 4289-4296,  
1014 10.1021/acs.est.6b05736, 2017.

1015 Song, M., Marcolli, C., Krieger, U. K., Zuend, A., and Peter, T.: Liquid-liquid phase separation  
1016 and morphology of internally mixed dicarboxylic acids/ammonium sulfate/water particles, *Atmos.*  
1017 *Chem. Phys.*, 12, 2691-2712, 10.5194/acp-12-2691-2012, 2012.

1018 Song, S., Gao, M., Xu, W., Shao, J., Shi, G., Wang, S., Wang, Y., Sun, Y., and McElroy, M. B.:  
1019 Fine particle pH for Beijing winter haze as inferred from different thermodynamic equilibrium  
1020 models, *Atmos. Chem. Phys. Discuss.*, 2018, 1-26, 10.5194/acp-2018-6, 2018.

1021 Sorooshian, A., Ng, N. L., Chan, A. W. H., Feingold, G., Flagan, R. C., and Seinfeld, J. H.:  
1022 Particulate organic acids and overall water-soluble aerosol composition measurements from the  
1023 2006 Gulf of Mexico Atmospheric Composition and Climate Study (GoMACCS), *Journal of*  
1024 *Geophysical Research-Atmospheres*, 112, 16, 10.1029/2007jd008537, 2007.

1025 Sorooshian, A., Murphy, S. M., Hersey, S., Bahreini, R., Jonsson, H., Flagan, R. C., and Seinfeld,  
1026 J. H.: Constraining the contribution of organic acids and AMS m/z 44 to the organic aerosol  
1027 budget: On the importance of meteorology, aerosol hygroscopicity, and region, *Geophys. Res.*  
1028 *Let.*, 37, 5, 10.1029/2010gl044951, 2010.

1029 Spaulding, R. S., Talbot, R. W., and Charles, M. J.: Optimization of a mist chamber (cofer  
1030 scrubber) for sampling water-soluble organics in air, *Environmental Science & Technology*, 36,  
1031 1798-1808, 10.1021/es011189x, 2002.

1032 Suarez-Bertoa, R., Zardini, A. A., and Astorga, C.: Ammonia exhaust emissions from spark  
1033 ignition vehicles over the New European Driving Cycle, *Atmospheric Environment*, 97, 43-53,  
1034 10.1016/j.atmosenv.2014.07.050, 2014.

1035 Sullivan, A. P., Weber, R. J., Clements, A. L., Turner, J. R., Bae, M. S., and Schauer, J. J.: A  
1036 method for on-line measurement of water-soluble organic carbon in ambient aerosol particles:  
1037 Results from an urban site, *Geophysical Research Letters*, 31, 10.1029/2004gl019681, 2004.

1038 Sun, K., Tao, L., Miller, D. J., Pan, D., Golston, L. M., Zondlo, M. A., Griffin, R. J., Wallace, H.  
1039 W., Leong, Y. J., Yang, M. M., Zhang, Y., Mauzerall, D. L., and Zhu, T.: Vehicle Emissions as an  
1040 Important Urban Ammonia Source in the United States and China, *Environmental Science &*  
1041 *Technology*, 51, 2472-2481, 10.1021/acs.est.6b02805, 2017.

1042 Updyke, K. M., Nguyen, T. B., and Nizkorodov, S. A.: Formation of brown carbon via reactions  
1043 of ammonia with secondary organic aerosols from biogenic and anthropogenic precursors,  
1044 *Atmospheric Environment*, 63, 22-31, 10.1016/j.atmosenv.2012.09.012, 2012.

1045 Van Damme, M., Clarisse, L., Heald, C. L., Hurtmans, D., Ngadi, Y., Clerbaux, C., Dolman, A.  
1046 J., Erisman, J. W., and Coheur, P. F.: Global distributions, time series and error characterization

1047 of atmospheric ammonia (NH<sub>3</sub>) from IASI satellite observations, *Atmos. Chem. Phys.*, 14, 2905-  
1048 2922, 10.5194/acp-14-2905-2014, 2014.

1049 Warner, J. X., Wei, Z. G., Strow, L. L., Dickerson, R. R., and Nowak, J. B.: The global  
1050 tropospheric ammonia distribution as seen in the 13-year AIRS measurement record, *Atmos.*  
1051 *Chem. Phys.*, 16, 5467-5479, 10.5194/acp-16-5467-2016, 2016.

1052 Warner, J. X., Dickerson, R. R., Wei, Z., Strow, L. L., Wang, Y., and Liang, Q.: Increased  
1053 atmospheric ammonia over the world's major agricultural areas detected from space, *Geophysical*  
1054 *Research Letters*, 44, 2875-2884, 10.1002/2016gl072305, 2017.

1055 Weber, R. J., Orsini, D., Daun, Y., Lee, Y. N., Klotz, P. J., and Brechtel, F.: A particle-into-liquid  
1056 collector for rapid measurement of aerosol bulk chemical composition, *Aerosol Science and*  
1057 *Technology*, 35, 718-727, 10.1080/02786820152546761, 2001.

1058 Weber, R. J., Lee, S., Chen, G., Wang, B., Kapustin, V., Moore, K., Clarke, A. D., Mauldin, L.,  
1059 Kosciuch, E., Cantrell, C., Eisele, F., Thornton, D. C., Bandy, A. R., Sachse, G. W., and Fuelberg,  
1060 H. E.: New particle formation in anthropogenic plumes advecting from Asia observed during  
1061 TRACE-P, *Journal of Geophysical Research-Atmospheres*, 108, 13, 10.1029/2002jd003112,  
1062 2003.

1063 Weber, R. J., Guo, H., Russell, A. G., and Nenes, A.: High aerosol acidity despite declining  
1064 atmospheric sulfate concentrations over the past 15 years, *Nature Geoscience*, 9, 282-+,  
1065 10.1038/ngeo2665, 2016.

1066 Whittington, B. I., Jiang, C. J., and Trimm, D. L.: Vehicle exhaust catalysis: I. The relative  
1067 importance of catalytic oxidation, steam reforming and water-gas shift reactions, *Catalysis Today*,  
1068 26, 41-45, 10.1016/0920-5861(95)00093-u, 1995.

1069 Xing, J., Pleim, J., Mathur, R., Pouliot, G., Hogrefe, C., Gan, C. M., and Wei, C.: Historical  
1070 gaseous and primary aerosol emissions in the United States from 1990 to 2010, *Atmos. Chem.*  
1071 *Phys.*, 13, 7531-7549, 10.5194/acp-13-7531-2013, 2013.

1072 Xu, L., Guo, H., Boyd, C. M., Klein, M., Bougiatioti, A., Cerully, K. M., Hite, J. R., Isaacman-  
1073 VanWertz, G., Kreisberg, N. M., Knote, C., Olson, K., Koss, A., Goldstein, A. H., Hering, S. V.,

1074 de Gouw, J., Baumann, K., Lee, S.-H., Nenes, A., Weber, R. J., and Ng, N. L.: Effects of  
1075 anthropogenic emissions on aerosol formation from isoprene and monoterpenes in the southeastern  
1076 United States, *Proceedings of the National Academy of Sciences of the United States of America*,  
1077 112, 37-42, 10.1073/pnas.1417609112, 2015a.

1078 Xu, L., Suresh, S., Guo, H., Weber, R. J., and Ng, N. L.: Aerosol characterization over the  
1079 southeastern United States using high-resolution aerosol mass spectrometry: spatial and seasonal  
1080 variation of aerosol composition and sources with a focus on organic nitrates, *Atmos. Chem. Phys.*,  
1081 15, 7307-7336, 10.5194/acp-15-7307-2015, 2015b.

1082 Xu, L., Guo, H. Y., Weber, R. J., and Ng, N. L.: Chemical Characterization of Water-Soluble  
1083 Organic Aerosol in Contrasting Rural and Urban Environments in the Southeastern United States,  
1084 *Environmental Science & Technology*, 51, 78-88, 10.1021/acs.est.6b05002, 2017.

1085 Yao, X. H., Hu, Q. J., Zhang, L. M., Evans, G. J., Godri, K. J., and Ng, A. C.: Is vehicular emission  
1086 a significant contributor to ammonia in the urban atmosphere?, *Atmospheric Environment*, 80,  
1087 499-506, 10.1016/j.atmosenv.2013.08.028, 2013.

1088 You, Y., Renbaum-Wolff, L., and Bertram, A. K.: Liquid-liquid phase separation in particles  
1089 containing organics mixed with ammonium sulfate, ammonium bisulfate, ammonium nitrate or  
1090 sodium chloride, *Atmos. Chem. Phys.*, 13, 11723-11734, 10.5194/acp-13-11723-2013, 2013.

1091 You, Y., Kanawade, V. P., de Gouw, J. A., Guenther, A. B., Madronich, S., Sierra-Hernandez, M.  
1092 R., Lawler, M., Smith, J. N., Takahama, S., Ruggeri, G., Koss, A., Olson, K., Baumann, K., Weber,  
1093 R. J., Nenes, A., Guo, H., Edgerton, E. S., Porcelli, L., Brune, W. H., Goldstein, A. H., and Lee,  
1094 S. H.: Atmospheric amines and ammonia measured with a chemical ionization mass spectrometer  
1095 (CIMS), *Atmos. Chem. Phys.*, 14, 12181-12194, 10.5194/acp-14-12181-2014, 2014a.

1096 You, Y., Smith, M. L., Song, M., Martin, S. T., and Bertram, A. K.: Liquid-liquid phase separation  
1097 in atmospherically relevant particles consisting of organic species and inorganic salts, *International  
1098 Reviews in Physical Chemistry*, 33, 43-77, 10.1080/0144235x.2014.890786, 2014b.

1099 You, Y., and Bertram, A. K.: Effects of molecular weight and temperature on liquid-liquid phase  
1100 separation in particles containing organic species and inorganic salts, *Atmos. Chem. Phys.*, 15,  
1101 1351-1365, 10.5194/acp-15-1351-2015, 2015.

1102 Yu, H., and Lee, S. H.: Chemical ionisation mass spectrometry for the measurement of  
1103 atmospheric amines, *Environ. Chem.*, 9, 190-201, 10.1071/en12020, 2012.

1104 Zhang, H. F., Yee, L. D., Lee, B. H., Curtis, M. P., Worton, D. R., Isaacman-VanWertz, G.,  
1105 Offenberg, J. H., Lewandowski, M., Kleindienst, T. E., Beaver, M. R., Holder, A. L., Lonneman,  
1106 W. A., Docherty, K. S., Jaoui, M., Pye, H. O. T., Hu, W. W., Day, D. A., Campuzano-Jost, P.,  
1107 Jimenez, J. L., Guo, H. Y., Weber, R. J., de Gouw, J., Koss, A. R., Edgerton, E. S., Brune, W.,  
1108 Mohr, C., Lopez-Hilfiker, F. D., Lutz, A., Kreisberg, N. M., Spielman, S. R., Hering, S. V., Wilson,  
1109 K. R., Thornton, J. A., and Goldstein, A. H.: Monoterpenes are the largest source of summertime  
1110 organic aerosol in the southeastern United States, *Proceedings of the National Academy of*  
1111 *Sciences of the United States of America*, 115, 2038-2043, 10.1073/pnas.1717513115, 2018.

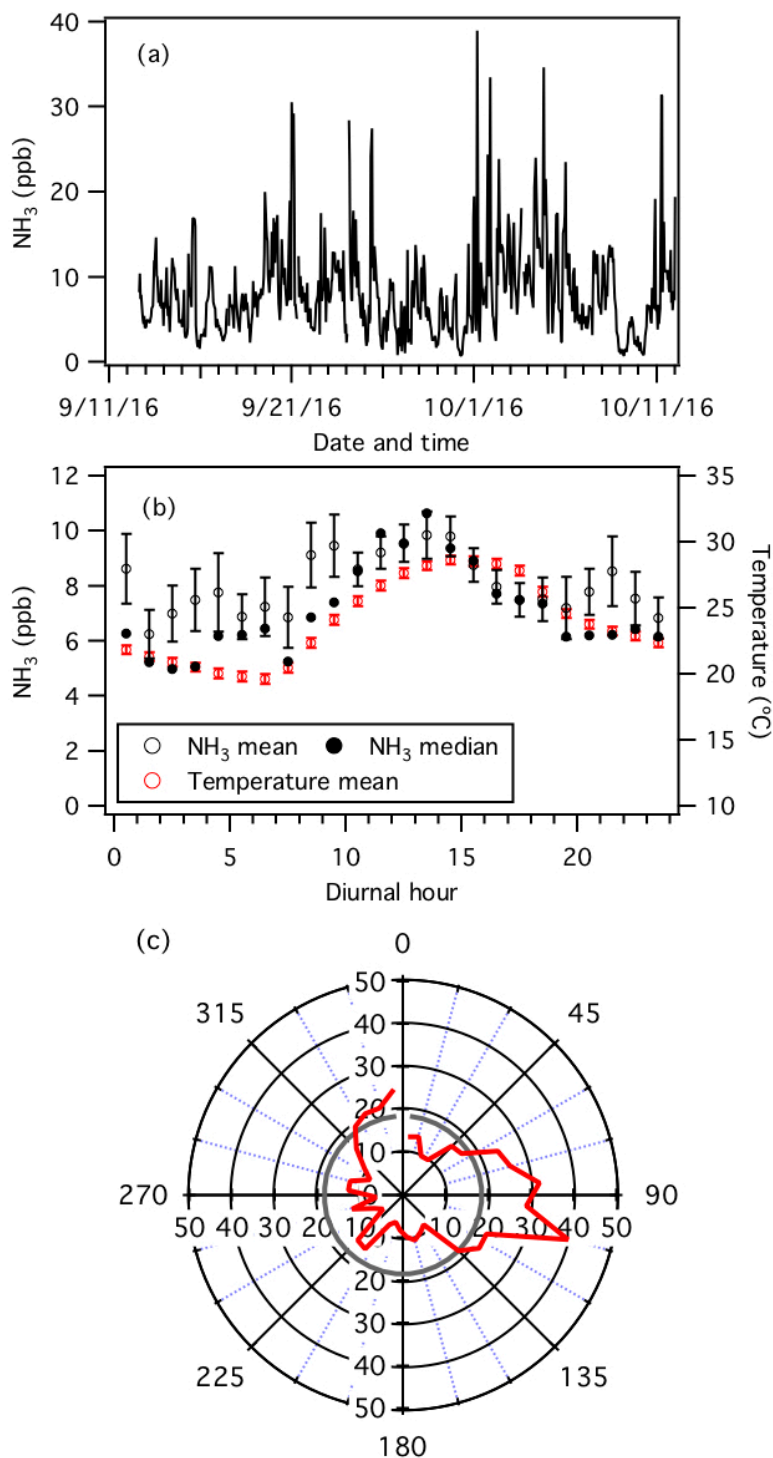
1112 Zuend, A., Marcolli, C., Luo, B. P., and Peter, T.: A thermodynamic model of mixed organic-  
1113 inorganic aerosols to predict activity coefficients, *Atmos. Chem. Phys.*, 8, 4559-4593,  
1114 10.5194/acp-8-4559-2008, 2008.

1115 Zuend, A., Marcolli, C., Booth, A. M., Lienhard, D. M., Soonsin, V., Krieger, U. K., Topping, D.  
1116 O., McFiggans, G., Peter, T., and Seinfeld, J. H.: New and extended parameterization of the  
1117 thermodynamic model AIOMFAC: calculation of activity coefficients for organic-inorganic  
1118 mixtures containing carboxyl, hydroxyl, carbonyl, ether, ester, alkenyl, alkyl, and aromatic  
1119 functional groups, *Atmos. Chem. Phys.*, 11, 9155-9206, 10.5194/acp-11-9155-2011, 2011.

1120 Zuend, A., Marcolli, C., Luo, B. P., and Peter, T.: A thermodynamic model of mixed organic-  
1121 inorganic aerosols to predict activity coefficients (vol 8, pg 4559, 2008), *Atmos. Chem. Phys.*, 12,  
1122 10075-10075, 10.5194/acp-12-10075-2012, 2012.

1123



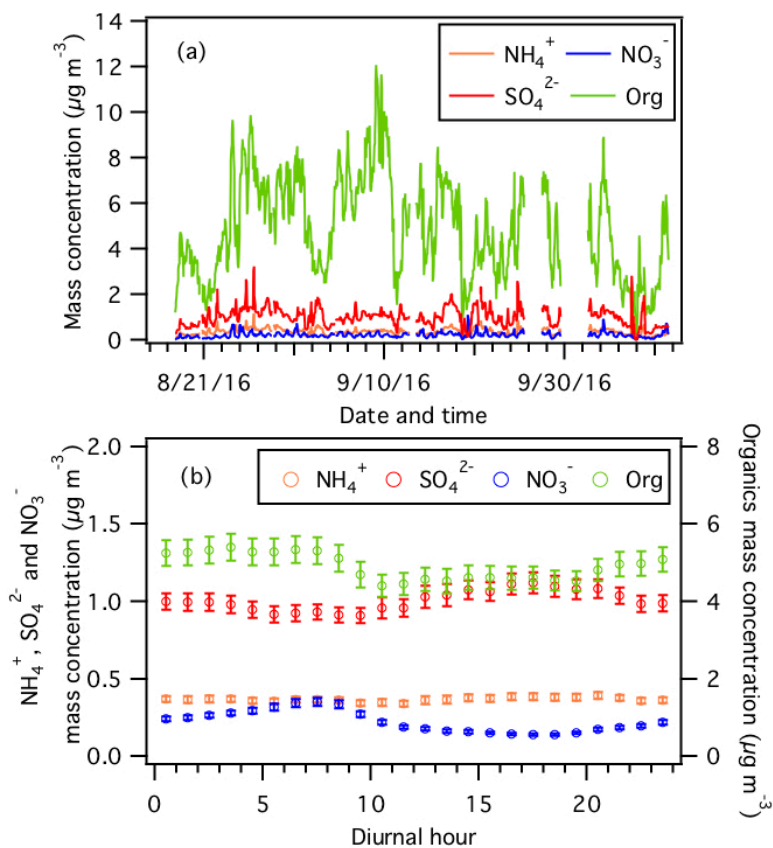


1124

1125 **Figure 1:** Measurements by the NH<sub>3</sub>-CIMS during the second half of the study. (a) Time series of  
 1126 NH<sub>3</sub> concentration. The data is displayed as 1-hour averages. (b) Diurnal profiles of NH<sub>3</sub>  
 1127 concentration (mean and median) and temperature. Error bars shown are the standard errors. Dates  
 1128 and times displayed are local time. All the concentrations represent averages in 1-hour intervals

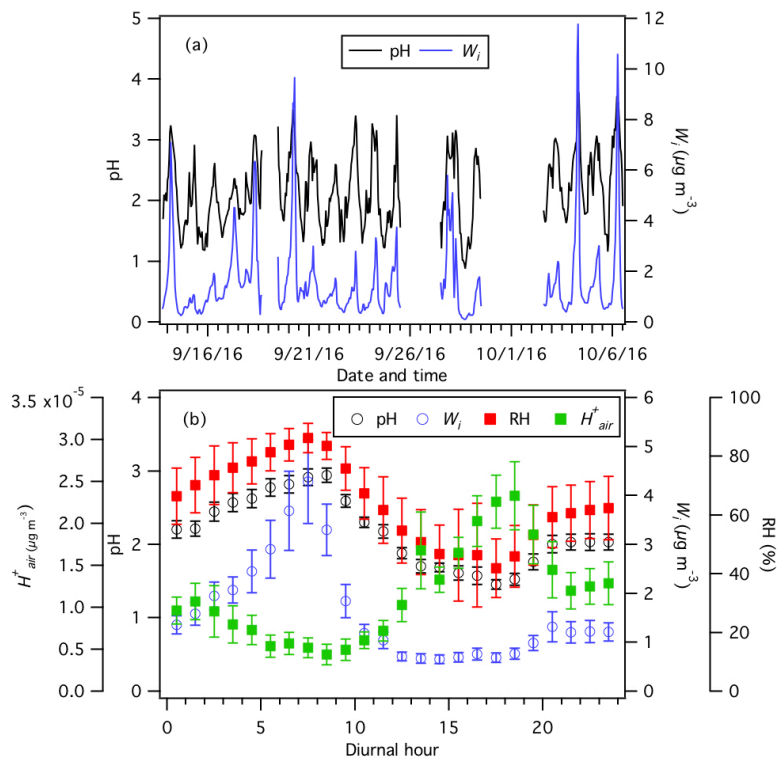
1129 and the standard errors are plotted as error bars. (c) Average  $\text{NH}_3$  concentration normalized to  
 1130 wind speed (i.e.,  $\text{NH}_3$  concentration (ppb)  $\times$  wind speed ( $\text{m s}^{-1}$ )) in each 10 degrees bin (red line).  
 1131 The average normalized  $\text{NH}_3$  concentration is shown as a grey line.

1132



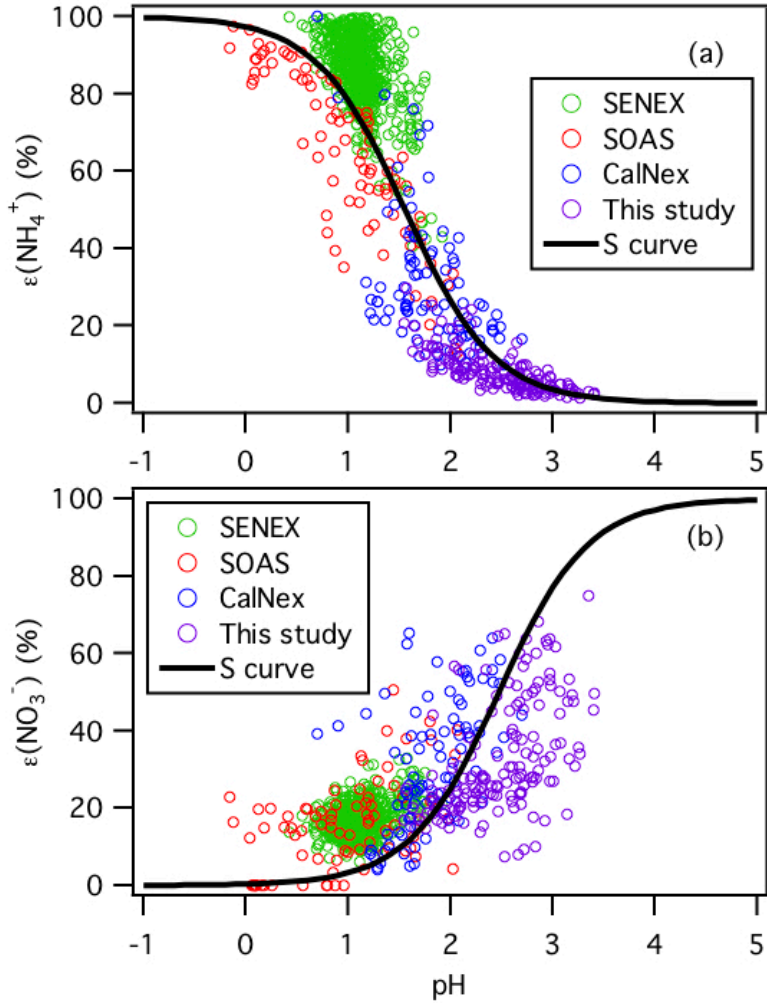
1133

1134 **Figure 2:** (a) Time series and (b) diurnal profiles of non-refractory  $\text{PM}_{10}$  species measured by the  
 1135 AMS. Error bars shown in panel (b) are the standard errors. Dates and times displayed are local  
 1136 time. All the mass concentrations shown here are obtained from scaling the raw data by 0.5. Refer  
 1137 to the text for details.



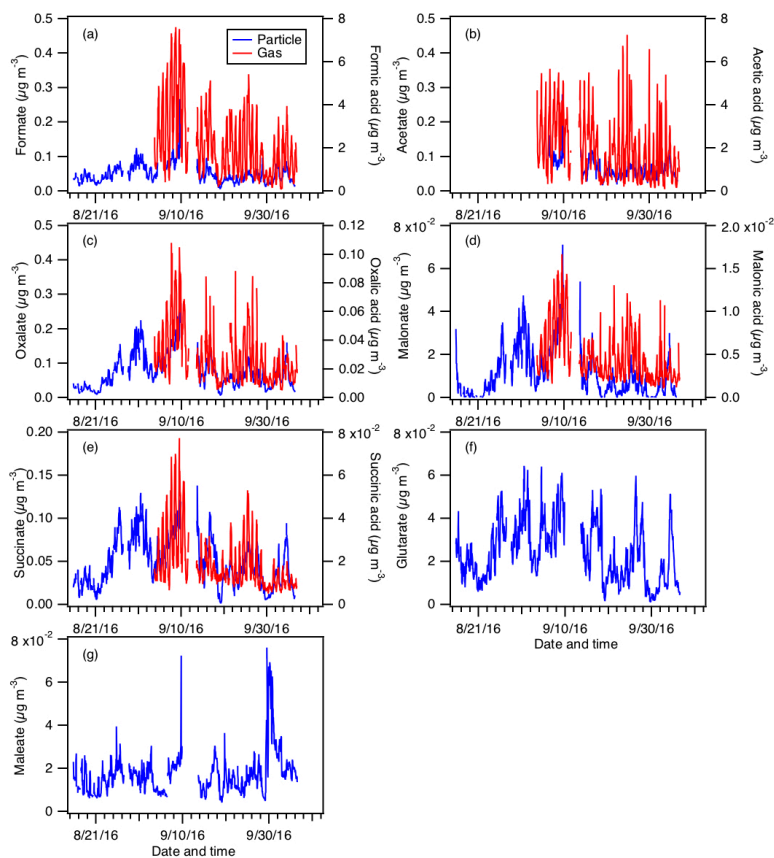
1138

1139 **Figure 3:** (a) Time series and (b) diurnal profiles of ISORROPIA-predicted  $\text{PM}_{10}$  pH and  $W_i$ . The  
 1140 diurnal profiles of RH and ISORROPIA-predicted  $H^+_{air}$  are also shown in panel (b). Dates and  
 1141 times displayed are local time. All the data shown here represent averages in 1-hour intervals.  
 1142 Error bars shown in panel (b) are the standard errors.



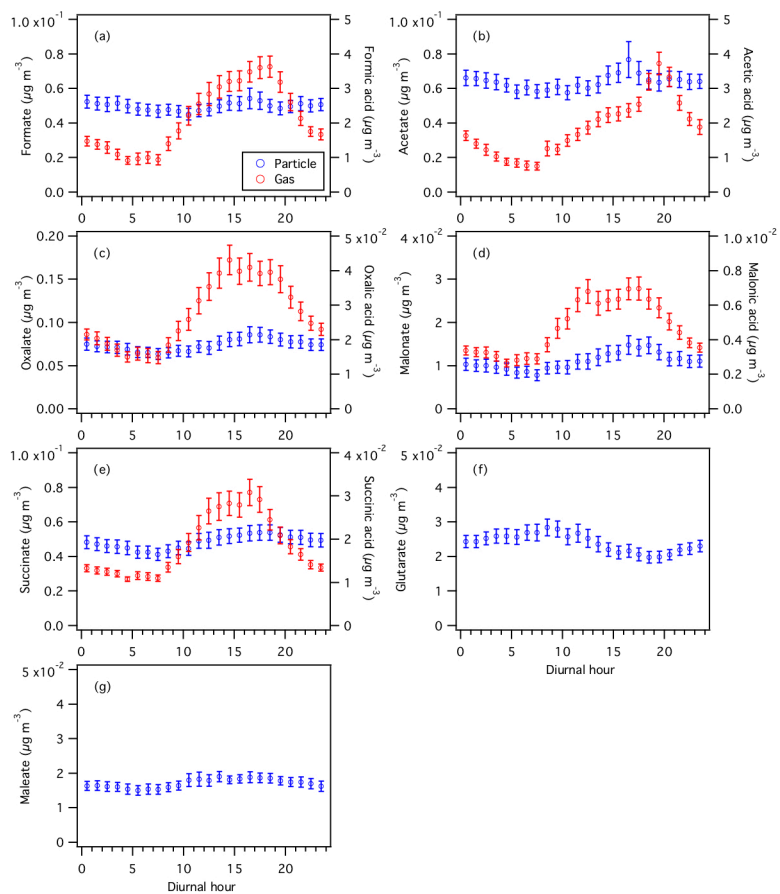
1143

1144 **Figure 4:** Analytically calculated S curves of  $\epsilon(\text{NH}_4^+)$  and  $\epsilon(\text{NO}_3^-)$  and ambient data plotted  
 1145 against ISORROPIA-predicted particle pH for this study, SENEX, SOAS and CalNex. For the  
 1146 ambient datasets, a narrow range of  $W_i$  (1 to 4  $\mu\text{g m}^{-3}$ ) and temperature (15 to 25  $^\circ\text{C}$ ) are selected  
 1147 to be close to the analytical calculation input (i.e.,  $W_i = 2.5 \mu\text{g m}^{-3}$  and temperature = 20  $^\circ\text{C}$ ).  
 1148 Similar to Guo et al. (2017a),  $\gamma_{\text{NH}_4^+} = 1$  and  $\gamma_{\text{H}^+-\text{NO}_3^-} = \sqrt{\gamma_{\text{H}^+}\gamma_{\text{NO}_3^-}} = 0.28$  are used for the  
 1149 analytically calculated S curves.



1150

1151 **Figure 5:** Particle- and gas-phase measurements of (a) formic, (b) acetic, (c) oxalic, (d) malonic,  
 1152 (e) succinic, (f) glutaric, and (g) maleic acids. Particle-phase measurements are shown on the left  
 1153 y axes, while gas-phase measurements are shown on the right y axes. Dates and times displayed  
 1154 are local time. Gas-phase measurements of glutaric and maleic acids are not available.

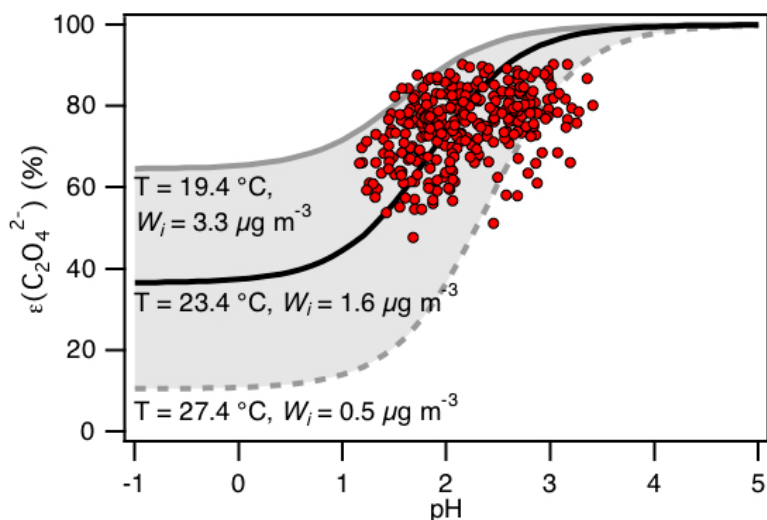


1155

1156 **Figure 6:** Diurnal profiles of particle- and gas-phase (a) formic, (b) acetic, (c) oxalic, (d) malonic,  
 1157 (e) succinic, (f) glutaric, and (g) maleic acids. Particle-phase measurements are shown on the left  
 1158 y axes, while gas-phase measurements are shown on the right y axes. All the data shown here  
 1159 represent averages in 1-hour intervals. Error bars shown are the standard errors.

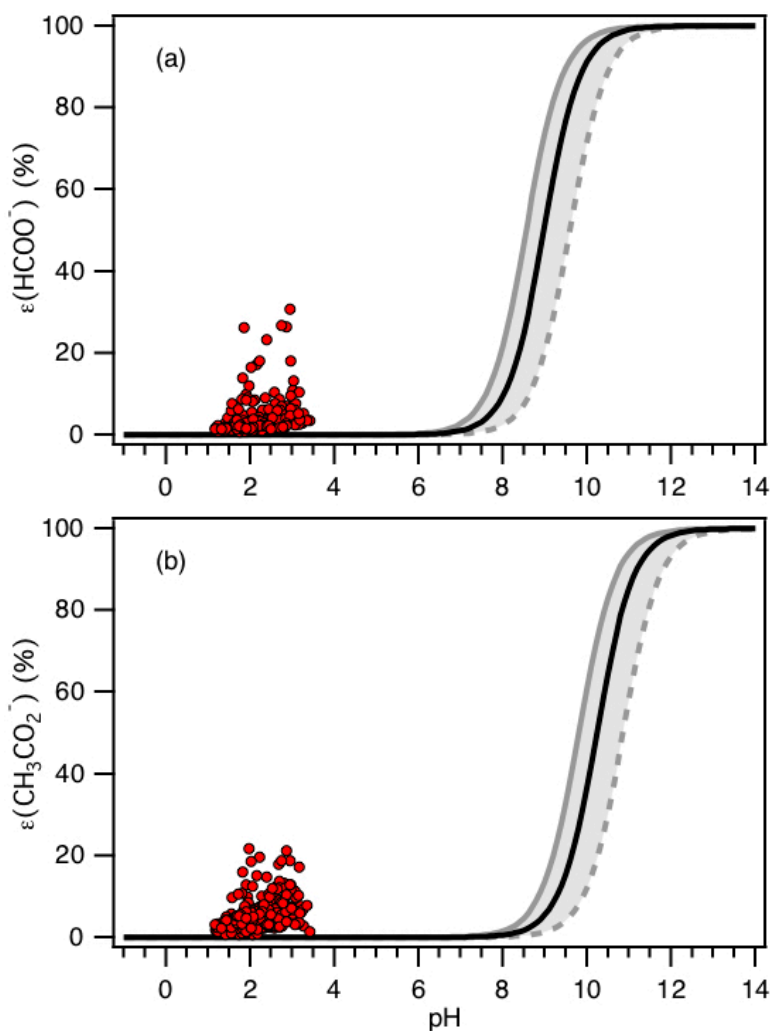
1160

1161



1162

1163 **Figure 7:** Analytically calculated S curve of  $\epsilon(\text{C}_2\text{O}_4^{2-})$  and ambient data from 13 September to 6  
 1164 October 2016 plotted against ISORROPIA-predicted particle pH. For the ambient data, a range in  
 1165  $W_i$  ( $0.5$  to  $4 \mu\text{g m}^{-3}$ ) and temperature ( $15$  to  $31 \text{ }^\circ\text{C}$ ) are chosen to be close to the analytically  
 1166 calculated outputs. For the analytically calculated S curves, we used  $\gamma_{\text{C}_2\text{H}_2\text{O}_4} = 0.0492$  (AIOMFAC  
 1167 predicted). We also assumed that  $\gamma_{\text{H}^+} + \gamma_{\text{C}_2\text{HO}_4^-} = \gamma_{\text{H}^+} + \gamma_{\text{NO}_3^-}$ , and used the ISORROPIA-predicted  
 1168  $\gamma_{\text{H}^+} + \gamma_{\text{NO}_3^-} = \sqrt{\gamma_{\text{H}^+} + \gamma_{\text{NO}_3^-}} = 0.265$ . The black line is the S curve calculated using the selected time  
 1169 period's average temperature ( $23.4 \pm 4.0 \text{ }^\circ\text{C}$ ) and  $W_i$  ( $1.6 \pm 1.7 \mu\text{g m}^{-3}$ ). The grey lines are S curves  
 1170 calculated using one standard deviation from the average temperature and  $W_i$  (i.e., temperature =  
 1171  $27.4 \text{ }^\circ\text{C}$  and  $W_i = 0.5 \mu\text{g m}^{-3}$  for dotted grey line, temperature =  $19.4 \text{ }^\circ\text{C}$  and  $W_i = 3.3 \mu\text{g m}^{-3}$  for  
 1172 solid grey line).



1173

1174 **Figure 8:** Analytically calculated S curves of  $\varepsilon(\text{HCOO}^-)$  and  $\varepsilon(\text{CH}_3\text{CO}_2^-)$  (solid black lines) and  
 1175 ambient data from 13 September to 6 October 2016 plotted against ISORROPIA-predicted particle  
 1176 pH (shown in panels (a) and (b), respectively). For the ambient data, a narrow range in  $W_i$  (0.5 to  
 1177  $4 \mu\text{g m}^{-3}$ ) and RH (20 to 90 %) is chosen to be close to the analytically calculated outputs. For the  
 1178 analytically calculated S curves, we used  $\gamma_{\text{HCOOH}} = 0.334$  and  $\gamma_{\text{CH}_3\text{COOH}} = 2.150$  (AIOMFAC  
 1179 predicted). We also assumed that  $\gamma_{\text{H}^+}\gamma_{\text{HCOO}^-} = \gamma_{\text{H}^+}\gamma_{\text{CH}_3\text{COO}^-} = \gamma_{\text{H}^+}\gamma_{\text{NO}_3^-}$ , and used the  
 1180 ISORROPIA-predicted  $\gamma_{\text{H}^+-\text{NO}_3^-} = \sqrt{\gamma_{\text{H}^+}\gamma_{\text{NO}_3^-}} = 0.265$ . The black lines are S curves calculated  
 1181 using the selected time period's average temperature ( $23.4 \pm 4.0 \text{ }^\circ\text{C}$ ) and  $W_i$  ( $1.6 \pm 1.7 \mu\text{g m}^{-3}$ ).  
 1182 The grey lines are S curves calculated using one standard deviation from the average temperature  
 1183 and  $W_i$  (i.e., temperature =  $27.4 \text{ }^\circ\text{C}$  and  $W_i = 0.5 \mu\text{g m}^{-3}$  for dotted grey line, temperature =  $19.4$   
 1184  $^\circ\text{C}$  and  $W_i = 3.3 \mu\text{g m}^{-3}$  for solid grey line).



1185 **Table 1:** Comparisons between different field campaigns for particle pH, major inorganic ions and  
 1186 gases and meteorological conditions. All pH values were calculated using ISORROPIA-II run in  
 1187 forward mode. These statistics were previously compiled by Guo et al. (2017a). Campaign  
 1188 acronyms used here stand for the California Research at the Nexus of Air Quality and Climate  
 1189 Change (CalNex), Southern Oxidant and Aerosol Study (SOAS), and Southeastern Nexus of Air  
 1190 Quality and Climate (SENEX).

Campaign	CalNex		SOAS	SENEX	This study
Type	Ground		Ground	Aircraft	Ground
PM cut size	PM <sub>1</sub>	PM <sub>2.5</sub> <sup>a</sup>	PM <sub>1</sub> &PM <sub>2.5</sub> <sup>b</sup>	PM <sub>1</sub>	PM <sub>1</sub>
Year	2010		2013	2013	2016
Season	(Early Summer)		Summer	Summer	Fall
Region/Location	SW US		SE US	SE US	SE US
SO <sub>4</sub> <sup>2-</sup> , μg m <sup>-3</sup>	2.86 ± 1.70	1.88 ± 0.69	1.73 ± 1.21	2.05 ± 0.80	1.6 ± 0.4
NO <sub>3</sub> <sup>-</sup> , μg m <sup>-3</sup>	3.58 ± 3.65	3.74 ± 1.53	0.08 ± 0.08	0.28 ± 0.09	0.20 ± 0.10
HNO <sub>3</sub> , μg m <sup>-3</sup>	6.65 ± 7.03	4.45 ± 3.59	0.36 ± 0.14	1.35 ± 0.66	0.50 ± 0.26
ε(NO <sub>3</sub> <sup>-</sup> )	39 ± 16 %	51 ± 18 %	22 ± 16 %	18 ± 6 %	26 ± 15 %
Total NO <sub>3</sub> <sup>-</sup> , μg m <sup>-3</sup>	10.22 ± 9.74	8.19 ± 3.89	0.45 ± 0.26	1.63 ± 0.70	0.70 ± 0.28
NH <sub>4</sub> <sup>+</sup> , μg m <sup>-3</sup>	2.06 ± 1.67	1.79 ± 0.65	0.46 ± 0.34	1.06 ± 0.25	0.40 ± 0.20
NH <sub>3</sub> , μg m <sup>-3</sup>	1.37 ± 0.90	0.75 ± 0.61	0.39 ± 0.25	0.12 ± 0.19	5.79 ± 3.67
ε(NH <sub>4</sub> <sup>+</sup> )	55 ± 25%	71 ± 19%	50 ± 25%	92 ± 11%	7 ± 5 %
Total NH <sub>4</sub> <sup>+</sup> , μg m <sup>-3</sup>	3.44 ± 1.81	2.54 ± 0.89	0.78 ± 0.50	1.17 ± 0.81	6.19 ± 3.68
Na <sup>+</sup> , μg m <sup>-3</sup>	\	0.77 ± 0.39	0.03 ± 0.07	\	\
Cl <sup>-</sup> , μgm <sup>-3</sup>	\	0.64 ± 0.48	0.02 ± 0.03	\	0.01 ± 0.01
RH, %	79 ± 17	87 ± 9	74 ± 16	72 ± 9	69 ± 18
T, °C	18 ± 4	18 ± 3	25 ± 3	22 ± 3	24 ± 4
W <sub>i</sub> , μg m <sup>-3</sup>	13.9 ± 18.1	29.8 ± 20.7	5.1 ± 3.8	3.2 ± 2.8	1.6 ± 1.7
pH	1.9 ± 0.5	2.7 ± 0.3	0.9 ± 0.6	1.1 ± 0.4	2.2 ± 0.6
Reference	(Guo et al., 2017a)		(Guo et al., 2015)	(Xu et al., 2016)	This study

1191 <sup>a</sup>Only during the last week of CalNex.

1192 <sup>b</sup>PM<sub>2.5</sub> was sampled in the first half and PM<sub>1</sub> sampled in the second half of the study. Various  
 1193 parameters were similar in both cases. Crustal components were higher, but are overall generally  
 1194 in low concentrations so the differences had minor effects. For example, PM<sub>2.5</sub> Na<sup>+</sup> was 0.06 ±  
 1195 0.09 μg m<sup>-3</sup> and PM<sub>1</sub> Na<sup>+</sup> was 0.01 ± 0.01 μg m<sup>-3</sup>.